POLITECNICO DI TORINO
Repository ISTITUZIONALE

Crack Process Investigation in Gears Under Single Tooth Bending Fatigue Condition Using Infrared Thermography and 3D XFEM Numerical Models

Original
Crack Process Investigation in Gears Under Single Tooth Bending Fatigue Condition Using Infrared Thermography and 3D XFEM Numerical Models / Corsaro, L., Fraccaroli, L., Cura, F., Concli, F.. - In: FATIGUE & FRACTURE OF ENGINEERING MATERIALS & STRUCTURES. - ISSN 1460-2695. - ELETTRONICO. - 0:(2026), pp. 1-19. [10.1111/ffe.70431]

Availability:
This version is available at: 11583/3016440 since: 2026-10-08T13:50:19Z

Publisher:
Wiley

Published
DOI:10.1111/ffe.70431

Terms of use:

This article is made available under terms and conditions as specified in the corresponding bibliographic description in the repository

Publisher copyright

(Article begins on next page)

08 November 2026

Check for updates

Fatigue & Fracture of Engineering Materials & Structures

WILEY

FFEMS Fatigue & Fracture of Engineering Materials & Structures

ORIGINAL ARTICLE OPEN ACCESS

Crack Process Investigation in Gears Under Single Tooth Bending Fatigue Condition Using Infrared Thermography and 3D XFEM Numerical Models

Luca Corsaro[1] | Lorenzo Fraccaroli[2] | Francesca Maria Curà[1] | Franco Concli[2]

[1]Department of Mechanical and Aerospace Engineering (DIMEAS), Politecnico Di Torino, Torino, Italy | [2]Faculty of Engineering, Free University of Bozen-Bolzano, Bolzano, Italy

Correspondence: Luca Corsaro (luca.corsaro@polito.it)

Received: 13 May 2026 | **Revised:** 7 July 2026 | **Accepted:** 17 August 2026

Keywords: fatigue crack growth | gears | high cycle fatigue | infrared thermography | numerical models | thermal dissipation

ABSTRACT

The present study proposes a combined approach of infrared thermography and 3D XFEM numerical models for crack process investigation in mechanical components such as gears. Over the years, fatigue crack analysis based on energy dissipations in the form of heat generated during fatigue tests has been widely reported, although mainly limited to classical specimens. In this work, this approach is extended to gears under single tooth bending fatigue conditions, where thermal dissipations were acquired using two infrared cameras. Numerical models were developed to investigate the entire crack process, with a focus on both nucleation and propagation. Thermal dissipations, processed in terms of temperature evolution and localized heating, were combined with numerical results and macroscopic fractographies. The analysis, performed on three gear case studies, shows that the crack mechanism can be investigated through thermal dissipations, highlighting asymmetric crack propagation and its evolution when the crack is still internal to the gear.

1 | Introduction

To guarantee the safety and reliability of mechanical components, a clear understanding of fatigue crack processes, including nucleation and propagation, is required.

The study of fatigue cracks by means of dissipated energy as heat was originally proposed beginning in the 1970s, as reported in [1–3]. Over the years, infrared (IR) thermography has attracted significant interest for fatigue crack analysis. This is due to its main advantages, such as noncontact measurements, full-field capability, and real-time detection of thermal dissipations ahead of a crack. This resulted in a series of significant research activities, as evidenced in [4–7], aimed to investigate the process of crack nucleation and propagation in relation to temperature variations and local heating during fatigue tests. These thermal aspects were found to be sufficiently sensitive and accurate to detect, investigate, and monitor damage localization and crack initiation, as well as the current location of the fatigue crack tip. These studies were conducted on classical specimens, and the experimental observations indicated a characteristic temperature evolution during the fatigue tests. The temperature evolution presented an initial increase, subsequently stabilizing. At the onset of crack initiation, a sudden increase in surface temperature was observed. This temperature increment allows the estimation of the number of cycles associated with crack nucleation and subsequent propagation. Several studies have also been proposed for the development of energy dissipation-based models, mainly aimed at analyzing crack growth, the plastic zone and the heat energy dissipated during the crack process. Examples of such studies were reported in [8–19]. More in detail, analytical models were developed to analyze the propagation of fatigue cracks, incorporating mechanical, cyclic, and fatigue properties, or length parameter to predict the crack growth rate.

This is an open access article under the terms of the Creative Commons Attribution License, which permits use, distribution and reproduction in any medium, provided the original work is properly cited.

© 2026 The Author(s). *Fatigue & Fracture of Engineering Materials & Structures* published by John Wiley & Sons Ltd.

Summary

- Crack process investigation in gears under STBF tests and HCF conditions.
- Crack growth mechanism analysis in high cycle fatigue conditions.
- 3D XFEM numerical models for crack nucleation and propagation processes.
- Internal and asymmetric crack detection through thermal dissipations.

Other models were formulated to analyze the energy generated in front of a fatigue crack, or to determine the temperature increase near the crack tip under fatigue loading. In particular, the application of IR Thermography was utilized during fatigue tests for experimental measurements with the aim of comparing the numerical results, as demonstrated in [13, 15, 16, 18, 19]. Throughout the years, the adoption of IR thermography for fatigue cracks analysis was also expanded across various materials and applications, as evidenced by the use of composite materials in [20]. It is evident, on the basis of the aforementioned considerations, that the study of fatigue cracks with dissipated energy is of significant relevance. However, most of the existing literature on this topic focuses on classical specimens, particularly when thermal dissipations are acquired with IR thermography. Only a limited number of studies, such as [21] and [22], have extended this approach to real structures or mechanical components. In [21], the authors proposed an approach based on different thermographic techniques for continuous and noncontact monitoring of fatigue cracks, enabling instantaneous evaluation and extending its applicability to structural components. In [22], a preliminary application of IR thermography for the analysis of crack propagation in gears was proposed, with the aim of investigating different failure modes such as fail-safe and catastrophic failures.

Over the years, the topic of fatigue crack growth focused on mechanical components with complex functionality and geometry has resulted in the development of numerical models to improve their analysis. Regarding the prediction of crack growth life in gear bending fatigue, numerous researchers had investigated both crack propagation life and crack growth trajectories using different numerical approaches, including eXtended Finite Element Method (XFEM) [23–25] and FEM [26–28]. The XFEM was developed in the late 1990s and is based on the partition of unity concept. This approach enriches classical finite element method (FEM) approximations with specific functions, allowing the representation of crack-tip singularities and displacement discontinuities across crack faces [29]. In conventional FEM analyses, the accurate representation of such discontinuities generally requires complex and computationally demanding remeshing procedures. XFEM overcomes this limitation, allowing crack growth to be simulated under various loading conditions without updating the mesh during propagation. This capability is achieved by introducing additional degrees of freedom at nodes in the vicinity of the crack front and by employing enrichment functions, allowing the crack to propagate independently of the underlying mesh. Consequently, XFEM is particularly well suited for problems involving complex geometries and nonuniform loading, where traditional FEM would require frequent remeshing operations [30]. In recent decades, fatigue design methodologies have often taken into account multiaxial critical plane criteria for HCF applications [31–33]. This framework generally enables the evaluation of both crack initiation and orientation of the plane along which early crack propagation occurs. Several approaches have been proposed in the literature to model the underlying mechanisms, depending on the stress state or the physical conditions governing crack initiation. Representative examples include the Findley criterion [34], the Crossland criterion [35], the Fatemi–Socie criterion [36], and the Smith–Watson–Topper (SWT) criterion [37, 38]. Thus, the use of these methodologies is of significant interest in the characterization of fatigue crack behavior, facilitating accurate descriptions of the crack process.

In this study, IR thermography was adopted for the acquisition of thermal dissipations produced from gears subjected to single tooth bending fatigue (STBF) conditions. Subsequently, the thermal dissipations were processed in terms of temperature evolutions and local heating at the crack tip, considered as representative of the entire fatigue crack evolution process. The experimental observations in terms of thermal dissipations were also compared with those reported in the literature for specimens, in order to identify differences in mechanical components such as gears. Dedicated 3D XFEM numerical models were run to compare the results coming from experimental campaigns.

Furthermore, an analysis of the crack evolution path was conducted, basing on local heating over thermal maps, when the crack was still inside the gear. In addition, fracture surfaces were investigated for the purpose of validating these results. Three distinct case studies in terms of gear geometry and material were analyzed, testing the gears under different loading conditions during the STBF tests.

2 | The Bending Stress Field in Gears: Theoretical Background

The probability of bending fatigue failure is typically evaluated according to ISO 6336-3 and ANSI/AGMA 2101-D04 [39, 40], as these standards adopt conservative design criteria. From this perspective, STBF testing can be considered an effective and reliable experimental approach compared with tests performed on notched specimens or operating gears.

According to ISO 6336-3 [39], the maximum tensile stress σ_F at the tooth root is responsible for tooth bending fatigue failures and can therefore be considered as a critical damage parameter. It is thus well established that, under STBF loading conditions, the tooth failure tends to occur in the tooth root region. However, an evaluation based only on ISO 6336-3 [39] considerations does not provide the crack nucleation position along the face width to be determined a priori, as also discussed in [41]. Numerous experimental studies, together with the experimental results of the present work, have shown that crack nucleation does not occur in the gear side faces, but is generally shifted toward a more internal region of the face width. These observations suggest that three-dimensional effects play a significant

14602695, 0, Downloaded from https://onlinelibrary.wiley.com/doi/10.1111/ffe.70431 by Luca Corsaro - Politecnico Di Torino Sist. Bibl Del Polit Di Torino , Wiley Online Library on [08/10/2026]. See the Terms and Conditions (https://onlinelibrary.wiley.com/terms-and-conditions) on Wiley Online Library for rules of use; OA articles are governed by the applicable Creative Commons License

role in determining the actual crack initiation location [42]. In light of these findings, a finite element analysis was carried out to investigate the stress distribution at the tooth root along the gear thickness and to provide a numerical explanation of the experimentally observed behavior.

The numerical model adopted for this analysis is identical to the one that will be described in the following sections (see Section 4) devoted to crack nucleation and propagation.

In Figure 1, a simplified schematic of the gear subjected to an applied force is shown on the left-hand side; the axis along which the tooth root stress distribution was subsequently plotted is also highlighted. By analyzing Figure 1, the distribution of tooth root stresses along the face width is nonuniform. In fact, principal stress peaks (see σ_{max} in Figure 1) are produced during tooth bending close to the lateral regions of the gear and not near the center of the face width. This behavior can be attributed to three-dimensional effects and edge effects arising from the different stiffness of the components involved in the STBF configuration and from the resulting load transfer between the punch and the gear tooth. Consequently, the crack nucleation point is expected in proximity of these stress peaks (see orange point in Figure 1) [43]. The percentage difference between the maximum stress value and the stress at the center of the gear width was found to be approximately 3.3%. The numerical simulation confirmed this behavior by highlighting the nonuniform stress distribution along the gear face width.

3 | Materials and Methods

3.1 | Samples

The aim of this study is to investigate the process of crack nucleation and propagation for a number of case studies of mechanical components, specifically gears. Moreover, the analysis was conducted through numerical and experimental activities.

A detailed description of the case studies is provided in Table 1, while Figure 2 illustrates an example of the gears used in the experimental activity.

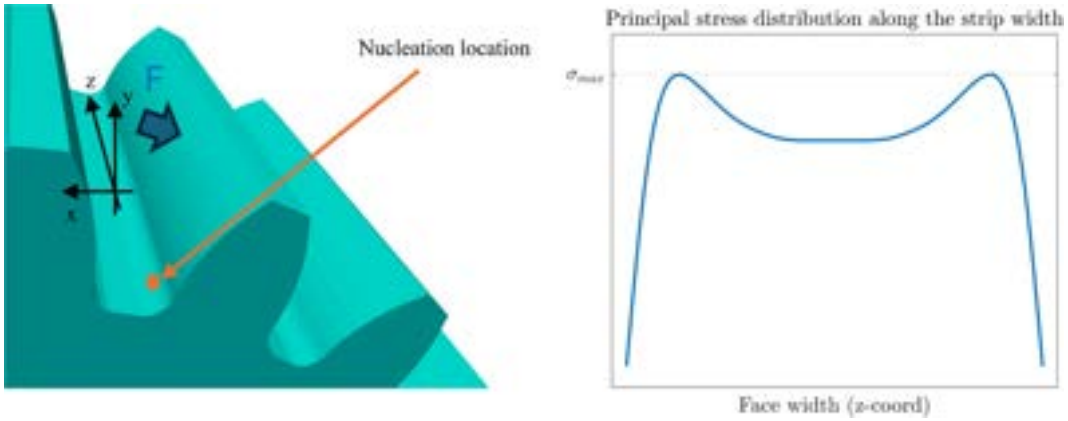

FIGURE 1 | Stress distribution at the tooth root. [Colour figure can be viewed at wileyonlinelibrary.com]

TABLE 1 | Gears: case studies.

Case study	Material and surface treatment	Geometry	Tooth root mechanical properties	ISO 6336 – part 3 standard factors [39]	SWT model parameters
Gear 1	18NiCrMo5 carburized steel ($CHD_{550}=0.5$ mm)	• $m_n=2.2$ mm • $z=30$ • $\alpha=17°$ • $w=20$ mm • $x=0.25$ mm	• $Rz=4.35\,\mu$m • $H=964$ HV • $E=240$ GPa	• $Y_S=1.59$ • $Y_F=1.75$	$\sigma'_f=4417$ $\varepsilon'_f=0.259$ $b=-0.13$ $c=-0.55$
Gear 2	20MnCr5 carburized steel ($CHD_{550}=0.6$ mm)	• $m_n=2.2$ mm • $z=30$ • $\alpha=17°$ • $w=20$ mm • $x=0.25$ mm	• $Rz=4.32\,\mu$m • $H=970$ HV • $E=210$ GPa	• $Y_S=1.59$ • $Y_F=1.75$	$\sigma'_f=4141$ $\varepsilon'_f=0.156$ $b=-0.14$ $c=-0.59$
Gear 3	20MnCr5 carburized steel ($CHD_{550}=0.7$ mm)	• $m_n=3$ mm • $z=20$ • $\alpha=20°$ • $w=28$ mm • $x=0$ mm	• $Rz=1.9\,\mu$m • $H=820$ HV • $E=210$ GPa	• $Y_S=1.82$ • $Y_F=1.77$	$\sigma'_f=3600$ $\varepsilon'_f=0.118$ $b=-0.11$ $c=-0.7$

14602695, 0, Downloaded from https://onlinelibrary.wiley.com/doi/10.1111/ffe.70431 by Luca Corsaro - Politecnico Di Torino Sist. Bibl Del Polit Di Torino , Wiley Online Library on [08/10/2026]. See the Terms and Conditions (https://onlinelibrary.wiley.com/terms-and-conditions) on Wiley Online Library for rules of use; OA articles are governed by the applicable Creative Commons License

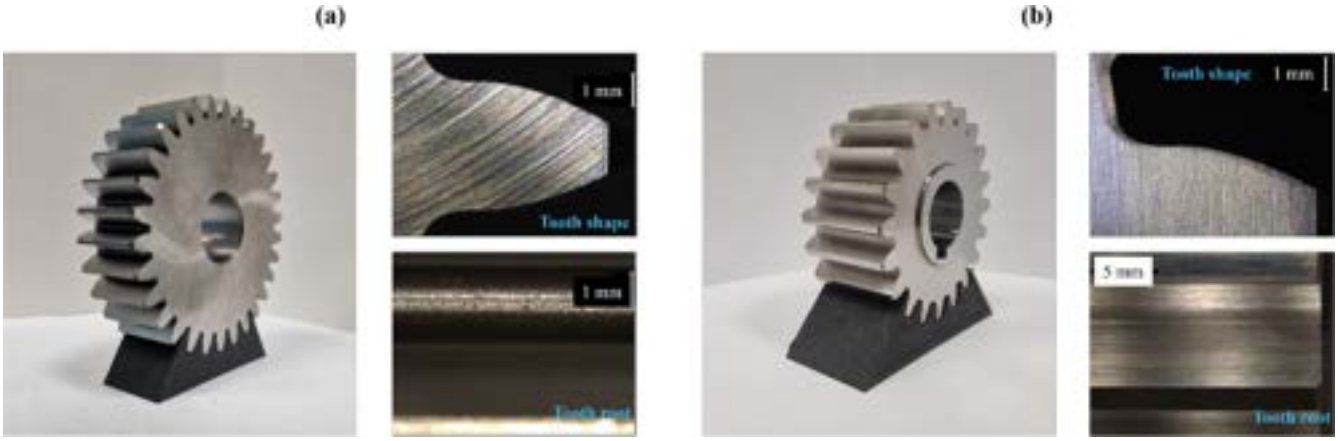

FIGURE 2 | Gears samples: (a) Gear 1 and Gear 2; (b) Gear 3. [Colour figure can be viewed at wileyonlinelibrary.com]

The columns of Table 1 report the case study nomenclature (first column: Gear 1, Gear 2, and Gear 3), the material and surface treatment of each tested gear (second column: 18NiCrMo5 steel for Gear 1, 20MnCr5 steel for Gear 2 and Gear 3; all subjected to a carburizing surface treatment with a case hardening depth reported in terms of CHD_{550}), the gear geometry (third column: two distinct gear geometries, one for Gear 1 and Gear 2 and another for Gear 3), the mechanical properties at the tooth root (fourth column: roughness and hardness) and the ISO 6336 – part 3 standard factors [39] (fifth column: tooth form factor, Y_F, and the stress correction factor, Y_S). The strain-life properties required for the SWT-based crack initiation analysis were estimated according to the Roessle–Fatemi procedure [44], a hardness-based approach developed for steels when dedicated strain-life fatigue data are not available. The available tooth root hardness values were used within this procedure, and the adopted parameter set was selected consistently with literature data for case-hardened gear steels [45]. This procedure has already been adopted in gear fatigue analyses, as reported for example in [46–49]. The adopted parameter values are reported in Table 1. To summarize, the study utilized three gears (Gear 1, Gear 2, and Gear 3). These were categorized into two distinct geometries, with Gear 1 and Gear 2 characterized by the same geometry and Gear 3 by a different one. Two materials were considered, 18NiCrMo5 for Gear 1 and 20MnCr5 for Gear 2 and Gear 3, both subjected to carburizing surface treatment.

In order to process the thermal emissions acquired during fatigue tests, the gear was coated with black paint, ensuring a known emissivity value of 0.95, as recommended in the reference tables [50].

3.2 | Experimental Setup for Bending Fatigue Test on Gears

The bending fatigue tests performed for each gear were conducted using the so-called STBF test configuration. The testing machine used in this activity was a resonance fatigue machine, which was capable of reaching a testing frequency of up to 174 Hz. Dedicated equipment was specifically designed to perform experimental fatigue tests under conditions of high testing frequency, with the objective of optimizing thermal emissions acquisition.

Figure 3 illustrates the experimental setup adopted during the SFBF tests. The STBF configuration ensured precise application of the load over the tested teeth near the upper point of single pair tooth contact [39], which represents the worst condition during the meshing of the gear. In order to reproduce this testing condition, the number of teeth between the interface parts (element n°4, see Figure 3) was selected according to the Wildhaber approach, as typically reported in the literature [51, 52]. Following this approach, the Wildhaber measurement, commonly used for gear quality control, is adapted for STBF testing. More in detail, the Wildhaber measurement is used to control the position of the load application so that it is located near the upper point of single pair tooth contact, as recommended by the Standard [39]. The evaluation depends on the gear geometry and on the number of teeth considered between the anvils. Consequently, the contact radius between the anvil and the loading elements was controlled through the configuration defined by the Wildhaber approach. In particular, the position of the contact was adjusted by selecting the appropriate number of teeth so that the contact radius was located as close as possible to the point of interest. This point, corresponding to the upper point of single pair tooth contact, was evaluated according to the relevant standard [39], and the testing configuration was calibrated accordingly to ensure that the load was applied in its proximity. In case of Gear 1 and Gear 2, a total of five teeth was required because of the similarity in gear geometry (refer to Table 1). In contrast, Gear 3 necessitated a total of three teeth.

The alignment between the gear teeth and the loading elements was ensured by means of calibrated positioning blocks. A first set of blocks was specifically designed to satisfy the conditions defined by the Wildhaber approach, allowing the correct positioning of the gear between the anvils near the upper point of single pair tooth contact. At the same time, this configuration fixed the position of the gear so that the contact point between the teeth and the anvils lay along the load application line, ensuring that the desired loading condition was correctly achieved. Then, a second set of calibrated blocks was

14602695, 0, Downloaded from https://onlinelibrary.wiley.com/doi/10.1111/ffe.70431 by Luca Corsaro - Politecnico Di Torino Sist. Bibl Del Polit Di Torino , Wiley Online Library on [08/10/2026]. See the Terms and Conditions (https://onlinelibrary.wiley.com/terms-and-conditions) on Wiley Online Library for rules of use; OA articles are governed by the applicable Creative Commons License

developed to ensure the correct positioning of the gear along the face width between the anvils. This configuration allowed the load to be uniformly distributed along the face width during the test. Consequently, proper contact conditions along the tooth width were ensured and the repeatability of the experimental setup was guaranteed. The gear under test was supported with a pin (element n°5, see Figure 3) during the STBF test, with the objective of guaranteeing the correct testing position, particularly in cases of high testing frequency. This element acts as a gear shaft, providing only support to the gear and allowing it to adapt its position. When the teeth are not in contact with the loading elements (element n°4, see Figure 3), the gear is free to rotate around the pin, since no mechanical constraints are present. Once contact between the teeth and the loading elements is established, the rotation of the gear is prevented, and the tooth is consequently loaded to reproduce STBF testing conditions in accordance with the Wildhaber approach. Consequently, the load received by the lower tooth (element n°7, see Figure 3) was slightly different compared to the corresponding load that acts on the upper tooth (element n°8, see Figure 3) because of the pin (element n°5, see Figure 2).

The crack propagation analysis was conducted using different nominal pulsating forces on the basis of the tested gear. Table 2 reports the testing conditions utilized in this activity. More in detail, each case study (first column: Gear 1, Gear 2, and Gear 3) was investigated under two different testing conditions (second column: Load 1 and Load 2). These testing conditions are illustrated in terms of maximum (third column: maximum nominal pulsating force) and minimum (fourth columns: minimum nominal pulsating force) loads during the STBF tests. The load levels were selected based on a preliminary estimation of the bending fatigue strength of the gears, performed according to the procedures reported in [39]. Two load levels were then defined within the finite life region, with the aim of operating under HCF conditions. The selected loads correspond to different force levels, thus generating different stress conditions at the tooth root. The fatigue tests were conducted by applying maximum and minimum loads corresponding to a load ratio (R, see Table 2) of 0.1, as generally adopted for the STBF configuration.

The thermal dissipations produced during the STBF tests were acquired by means of two identical IR cameras (element n°5, see Figure 3). Each IR camera is characterized by an IR resolution

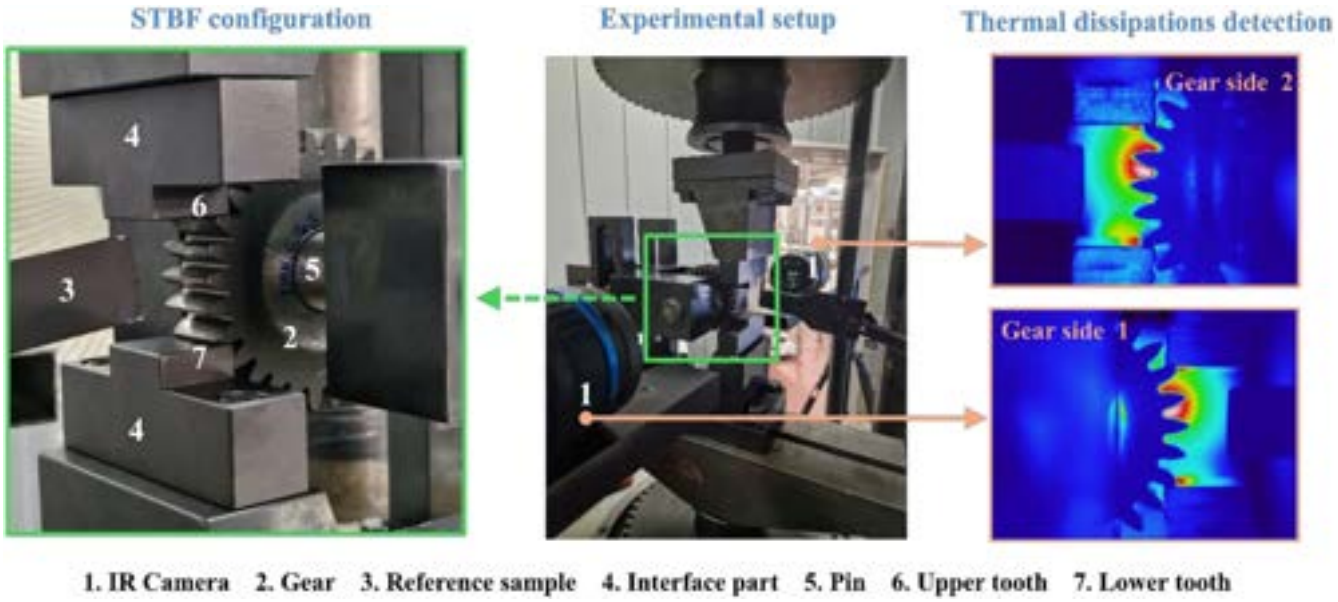

FIGURE 3 | Experimental setup during the STBF tests. [Colour figure can be viewed at wileyonlinelibrary.com]

TABLE 2 | Testing conditions during STBF tests.

Case study	Testing condition	Maximum nominal pulsating force (N)	Minimum nominal pulsating force (N)	Load ratio R
Gear 1	Load 1	−1800	−18,000	0.1
	Load 2	−2000	−20,000	0.1
Gear 2	Load 1	−1650	−16,500	0.1
	Load 2	−1700	−17,000	0.1
Gear 3	Load 1	−3450	−34,500	0.1
	Load 2	−3650	−36,500	0.1

14602695, 0, Downloaded from https://onlinelibrary.wiley.com/doi/10.1111/ffe.70431 by Luca Corsaro - Politecnico Di Torino Sist. Bibl Del Polit Di Torino , Wiley Online Library on [08/10/2026]. See the Terms and Conditions (https://onlinelibrary.wiley.com/terms-and-conditions) on Wiley Online Library for rules of use; OA articles are governed by the applicable Creative Commons License

of 640×480 pixels, a spectral range of 7.5–14 μm, a frame rate of 30 Hz, and a thermal sensitivity (NETD) lower than 30 mK at 30°C. The IR cameras were positioned at a distance of 0.17-m distant from the two later faces of the gear (Gear side 1 and Gear side 2, see Figure 3). Concerning the thermographic measurements, the thermal signal was processed in terms of relative temperature variation (ΔT). In order to monitor the environmental temperature during the STBF tests, a sample covered with black paint was located adjacent to the gear (element n°3, see Figure 3), and its absolute temperature evolution was recorded by the IR cameras. The absolute temperature signals of the gear were extracted from an area in proximity to the most stressed zone at the tooth root fillet, indicated in standard [39], to capture the thermal dissipations generated during the fatigue tests. Then, the relative temperature ΔT was obtained as the difference between the absolute temperature evolution of the tooth and that of the reference sample, ensuring a consistent evaluation of the relative temperature variation (ΔT), as commonly performed in the analysis of specimens.

3.3 | Thermal Dissipations Analysis for the Fatigue Crack Process Investigation

The topic of thermal dissipations during fatigue tests is well known in literature in case of classical specimens. Moreover, several studies have investigated fatigue crack growth in relation to the heat generated during experimental tests.

In case of classical specimens, the thermal dissipations produced during the fatigue tests may be investigated in terms of temperature evolutions and local heating events. Figure 4a presents a generic temperature evolution profile processed from thermal dissipations recorded with an IR camera during a fatigue test. The temperature evolution is extracted from the thermogram in a region of interest, typically located at the center of the specimen. This profile represents the temperature variations generated during crack formation throughout the fatigue test. In general, the temperature evolution is characterized by an initial heating phase, followed by a stabilized trend corresponding to a uniform heating of the specimen (see Figure 4a, stabilized trend). Subsequently, for load values that remain below the fatigue limit, the temperature evolution tends to stabilize (see Figure 4a, dashed red line). This is due to the fact that no fatigue damages occur during fatigue cycles, and the thermal dissipations are generated by intrinsic dissipations as anelastic phenomena or internal damping. In contrast, in tests where the applied load value exceeds the fatigue limit (see Figure 4a, solid red line), an additional temperature variation is observed (see Figure 4a, temperature variation [start temperature increment]), resulting in a subsequent rapid temperature increment immediately preceding material failure (see Figure 4a, temperature variation [peak]). In such cases, the predominant intrinsic dissipation mechanism is micro-plasticization or dislocation movements within the material, in comparison to cases with loading below the fatigue limit. These phenomena consequently lead to fatigue crack initiation and propagation, involving irreversible energy associated with plastic strains that is dissipated as heat. This results in localized heating at the tip of the crack, leading to temperature increments after the stabilized trend. As part of this analysis, local heating events that appear on the thermal maps of the thermogram are also considered during the investigation. These phenomena generally represent the final stage of crack propagation immediately before failure. In the specific case of specimens, the thermal dissipations detection can be easily performed by means of just one IR camera or thermocouples. This is because the specimen can be considered thin. As a result, the analysis is carried out independently of the position of the thermal camera.

On the other hand, for thick geometries such as gears, a different approach is required, as the phenomena under study may evolve

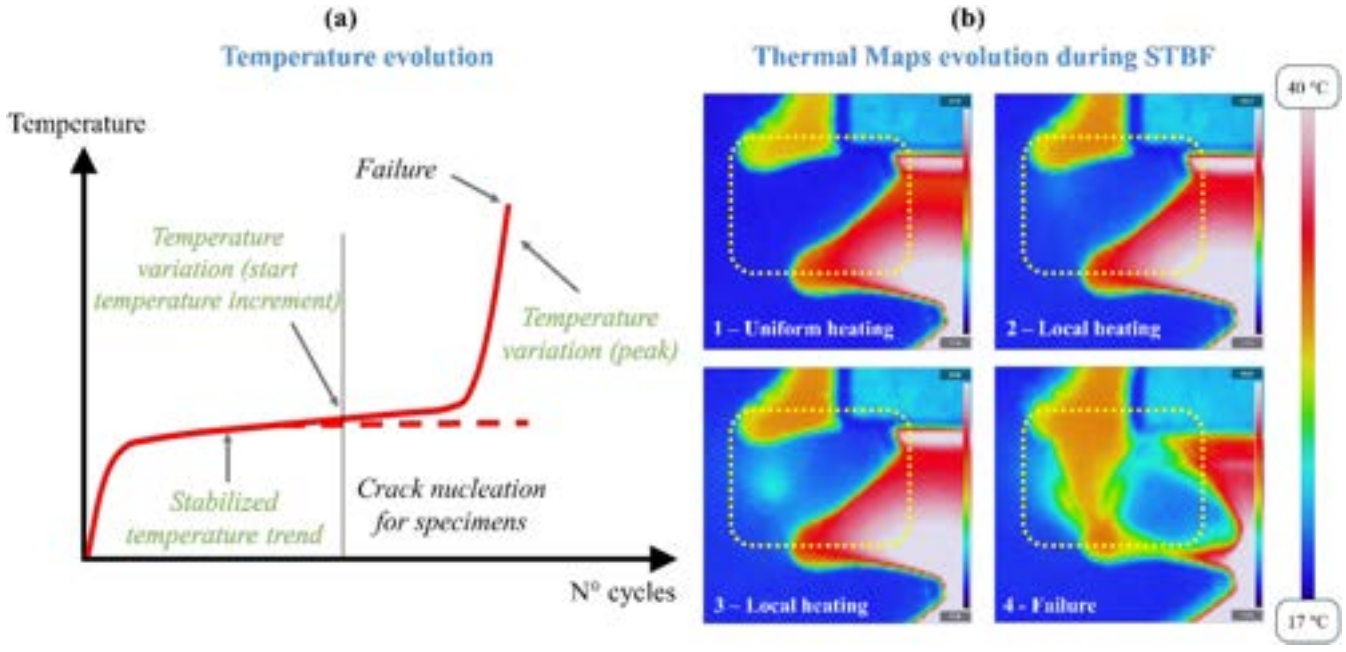

FIGURE 4 | Thermal dissipations: temperature evolution variations (a) and local heating over thermal maps for gears (b). [Colour figure can be viewed at wileyonlinelibrary.com]

14602695, 0, Downloaded from https://onlinelibrary.wiley.com/doi/10.1111/ffe.70431 by Luca Corsaro - Politecnico Di Torino Sist. Bibl Del Polit Di Torino , Wiley Online Library on [08/10/2026]. See the Terms and Conditions (https://onlinelibrary.wiley.com/terms-and-conditions) on Wiley Online Library for rules of use; OA articles are governed by the applicable Creative Commons License

in different directions along the face width of the geometry (see Section 2). For this aim, the thermal dissipations were acquired over the two lateral sides of the tested gear (Gear side 1 and Gear side 2, see Figure 3) by means of two IR cameras until the failure occurred. The thermal dissipations at the upper tooth (see element n°6 in Figure 3 of Section 3.2) were considered for the analysis, since the load involved during the STBF tests corresponded to the actual nominal pulsating force (see Section 3.2). In order to facilitate the analysis in case of gears, the following considerations can be drawn from a generic thermal map evolution (see Figure 4b) produced in case of gears under STBF. During the preliminary phase of the STBF tests, a uniform heating could be observed for the pixels involved in the tooth under investigation (see Figure 4b, thermal map: 1 – uniform heating). After that and near the conclusion of the STBF test, some local heating events may appear at the tooth root (see Figure 4b, thermal map: 2 – local heating). These phenomena are attributed to the dissipation of plastic strains in terms of heat at the crack tip near the external side. This enables the identification of the crack even when it remains internal to the gear and not externally visible. Subsequently, this local heating events increases in terms of both temperature increment and size once the tip of the crack moves toward the outer sides (see Figure 4b, thermal map: 3 – local heating). At the end, the failure of the tooth occurs (see Figure 4b, thermal map: 4 – failure). These thermal dissipations behavior of gears under STBF condition was found to be comparable to that described in [5] for specimens in terms of profile of the temperature evolution and local heating events. The only difference lies in identifying the entire crack process from temperature variations that occur during the temperature evolution. In specimens, the crack process can be identified by observing temperature variations and local heating events during the fatigue test, in accordance with [4–7]. Crack nucleation is associated with a deviation from the stabilized temperature trend (see Figure 4a, crack nucleation from specimen) and local heating events can then be detected over the surface of the specimen as a consequence of the propagation process. On the other hand, in the context of gears subjected to STBF testing, it is difficult to detect the entire crack process directly from temperature variations along the temperature evolution or local heating events dissipated from the external sides. This is because crack nucleation occurs along the face width of the geometry (see Section 2), which can make it difficult to detect through temperature evolution. In addition, the propagation exhibits an asymmetric distribution toward the external sides, as the nucleation point is not centrally located along the face width (see Section 2). Thus, the thermal dissipations observed during the STBF test are characterized by uniform heating with a quite stable temperature evolution trend, followed by temperature variations (in terms of deviation from the stable trend or temperature peaks) and several local heating events. Furthermore, as the crack tip approaches the outer side, the crack related phenomena become more pronounced. This is evidenced by local heating at the tooth root, which progressively increases in size and extends over a significant portion of the root region. It is important to note that this behavior is expected to follow distinct evolutions depending on the side of the gear analyzed, as a consequence of the different crack propagation along the face width of the gear.

For the specific purpose of crack process investigation in gears subjected to STBF conditions, thermal signals were extracted from a region of interest (ROI) located in proximity to the most stressed zone, the tensile tooth root, respectively, of the upper tested tooth. Due to the uniform heating of the tooth root during most of the STBF test, the size of the selected area has a limited influence on the average temperature value. Therefore, the dimensions of the selected area were chosen to effectively capture the onset of localized heating occurring at the tooth root fillet, as soon as it became detectable from the external side. Then, the same area size was adjusted for both lateral sides of the gear, so that thermal data were always extracted from regions with identical dimensions. This procedure was applied to both lateral sides of the gear. The environmental temperature was also extracted over the reference sample (element n°3, see Figure 2). Consequently, the ΔT was considered as the temperature signal generated during the STBF test.

4 | Finite Element and Fatigue Crack Initiation and Growth Analysis

Fatigue crack growth (FCG) is commonly examined by distinguishing two principal phases: crack nucleation and crack propagation. Furthermore, as shown in [53], under HCF conditions the overall fatigue process is predominantly governed by the nucleation stage, with a markedly lower contribution from crack propagation. Consequently, engineering analyses have focused on the evaluation and prediction of crack initiation using approaches based either on conventional stress–life (S–N) relationships derived from empirical data or on more advanced models capable of capturing local material behavior and damage accumulation [54–56].

Figure 5 illustrates the numerical procedure adopted to estimate the total tooth bending fatigue life of the gear. The model consists of two interconnected phases. The first phase involves the analysis of a single fatigue loading cycle experienced by the tooth (or the gear) under STBF conditions. From this initial analysis, the stress and strain tensors required for the application of critical plane criteria are extracted. A strain–life approach is adopted to estimate the number of cycles to crack nucleation, specifically using the SWT criterion. In addition to the number of cycles, this criterion also provides information on the crack nucleation location (with reference to the mesh nodes) and on the orientation of the early crack propagation. This information is then used to define the initial crack location on the analyzed component. Once the initial crack position is established, an iterative loop is performed to propagate the crack, update the mesh, and refine it where necessary. This procedure is repeated until the appropriate iteration is reached, corresponding to the numerical failure of the component. The entire cycle was developed by the authors in Python and directly implemented within the software. The numerical algorithm can be found in Appendix.

4.1 | Finite Element Model: Crack Initiation Analysis

To determine the crack nucleation location and the corresponding theoretical number of cycles, it was necessary to compute the cyclic stress and strain tensors induced by the tooth bending cyclic load. These quantities were obtained

14602695, 0, Downloaded from https://onlinelibrary.wiley.com/doi/10.1111/ffe.70431 by Luca Corsaro - Politecnico Di Torino Sist. Bibl Del Polit Di Torino , Wiley Online Library on [08/10/2026]. See the Terms and Conditions (https://onlinelibrary.wiley.com/terms-and-conditions) on Wiley Online Library for rules of use; OA articles are governed by the applicable Creative Commons License

through a finite element analysis performed using the open-source software Salome-Meca/Code_Aster. The boundary conditions adopted for this simulation will be described in the following section, as they are identical for each analysis iteration. The geometry used for the numerical simulation was generated using the characteristic geometric parameters of the gears, as summarized in Table 1. A linear elastic material model was adopted for the FE analyses, in accordance with the HCF regime investigated in this work. The elastic parameters were assigned according to the material considered and are reported in Table 1. The case-hardened surface layer was not modeled as a separate material layer with depth-dependent mechanical properties. Its effect was considered through the experimentally available information reported in Table 1, namely, the case hardening depth and the tooth root hardness. Residual stresses induced by the case-hardening treatment were not explicitly included in the numerical model, since no experimental measurements of the residual stress profile were available for the investigated gears.

To ensure that the nominally generated geometry accurately represented the actual gear geometry under investigation, the real tooth profile was directly acquired from the samples (gears) used in STBF tests. This procedure allows additional checks on the reliability of the numerical simulation, since the use of a nonrepresentative geometry could prevent the model from reproducing the real mechanical behavior. This aspect is particularly critical given that the tooth root region is the most highly stressed and is employed in all subsequent numerical analyses and evaluations. For the acquisition of the tooth profile, a profilometer (SM Metrology System PGS200) was employed. To ensure the correct positioning of the gear during the measurement, a dedicated support was manufactured using 3D printing. Figure 6 shows the geometry, the mesh and the superposition of the nominal and measured profiles. As can be observed, the two profiles differ significantly. In particular, for the gear with module $m = 3$, the nominal tooth root fillet radius was 0.6 mm, whereas the experimentally measured radius was 1.25 mm. Conversely, for the gears with module $m = 2.2$, the measured fillet radius was consistent with the nominal one. This procedure made possible to perform the numerical simulations using an accurate geometry, thereby ensuring the reliability of the obtained results.

Once the 3D model was generated, the components were discretized through a mesh, with local refinement in the regions of greatest interest, namely, the contact area with the punch and the crack nucleation region. For each case, a mesh composed of tetrahedral elements was generated. The initial number of elements was approximately 200 k and 260 k for the gear with module $m = 2.2$ and module $m = 3$, respectively. It should be noted that, during the crack propagation analysis, the mesh is locally refined and coarsened; therefore, the total number of

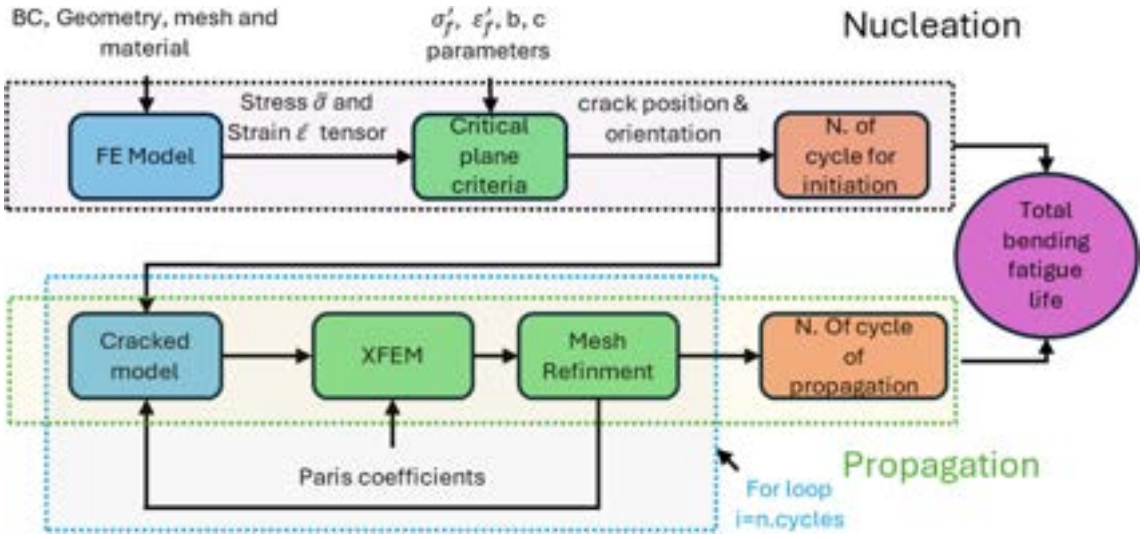

FIGURE 5 | Numerical algorithm. [Colour figure can be viewed at wileyonlinelibrary.com]

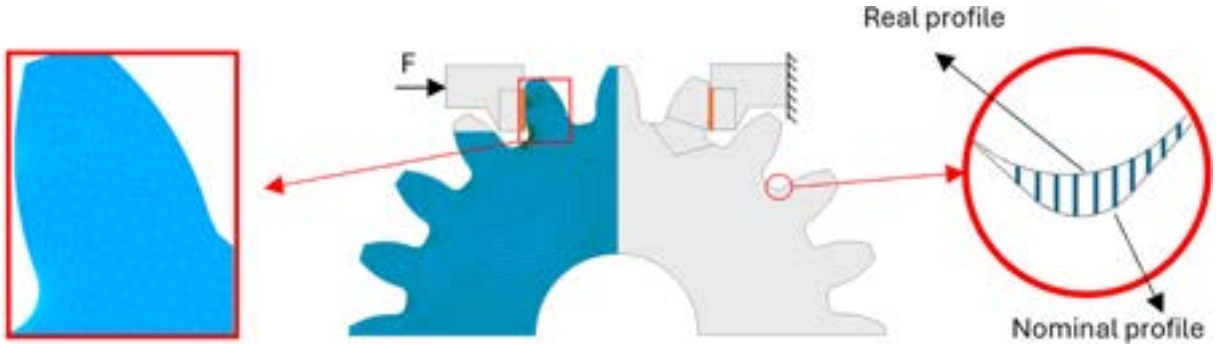

FIGURE 6 | Finite element model definition. [Colour figure can be viewed at wileyonlinelibrary.com]

14602695, 0, Downloaded from https://onlinelibrary.wiley.com/doi/10.1111/ffe.70431 by Luca Corsano - Politecnico Di Torino Sist. Bibl Del Polit Di Torino , Wiley Online Library on [08/10/2026]. See the Terms and Conditions (https://onlinelibrary.wiley.com/terms-and-conditions) on Wiley Online Library for rules of use; OA articles are governed by the applicable Creative Commons License

elements changes throughout the simulation. The minimum element size adopted for each case was determined through a sensitivity analysis performed on the Von Mises stresses at the tooth root fillet. Subsequently, the first analysis was carried out by reproducing the experimental STBF test conditions. The maximum element size in the regions of interest, such as the punch contact area and the tooth root fillet radius, was set to $a = 0.25\,\text{mm}$.

To reproduce the STBF test conditions, appropriate boundary conditions were imposed. As illustrated in Figure 6, surface-to-surface contact interactions, highlighted in orange, were defined between the punch surfaces and the corresponding tooth flanks. A cyclic force F was applied to the loading punch, in the same direction as in the experimental setup, whereas the opposite punch was used as a support. The support punch was fully constrained to reproduce its fixed condition in the test rig. The gear was constrained at the central bore, where the supporting pin is located in the experimental setup. This constraint prevents the translational motion of the gear while allowing its rotation around the axis of the central bore. In this way, the load was transferred to the gear tooth through the contact interaction between the loading punch and the tooth flank, while the support punch and the central bore constraint reproduced the experimental boundary conditions. In the numerical model, contact interactions were handled using the standard continuous contact formulation available in Code_Aster, based on an augmented Lagrangian approach. The contact constraints were enforced through Lagrange multipliers, providing a robust treatment of the contact problem, although this may increase the computational cost of the simulation.

4.2 | Fatigue Crack Initiation Model

As mentioned in the previous section, the SWT criterion was employed to estimate the number of cycles to crack nucleation and to determine both the location and the orientation of the early crack propagation [37, 38]. This criterion identifies the critical plane as the plane experiencing the maximum strain range $\Delta\epsilon_{n,max}$ during the cyclic load. The fatigue life associated with the damage referred to this critical plane is described by the following equation:

$$\frac{\Delta\epsilon_{n,max}}{2} \cdot \sigma_{\text{n,max}} = \frac{\sigma_f'^{\,2}}{E} \cdot (2N)^{2b} + \sigma_f' \cdot \epsilon_f' \cdot (2N)^{b+c} \tag{1}$$

where E is the elastic modulus, σ_f' is the fatigue strength coefficient, b is the fatigue strength exponent, ϵ_f' is the fatigue ductility coefficient, and c is the fatigue ductility exponent. The left-hand side of the equation represents the fatigue indicator parameter calculated using the SWT criterion. Because it is based on the combined effect of the normal strain amplitude and the maximum normal stress acting on the critical plane, the SWT criterion is particularly suitable for fatigue problems dominated by tensile/normal stress components, such as tooth root bending fatigue, where crack initiation is expected to occur mainly under mode-I–dominated conditions [45]. Because it relies on the combined evaluation of stress and strain, similarly to the Fatemi–Socie criterion [36], this model is applicable to both HCF and low-cycle fatigue (LCF) analysis. The strain life properties necessary for the cyclic analysis were found thanks to the method described in [46].

4.3 | Fatigue Crack Propagation Model

The crack propagation phase was developed directly within the FEM software by means of XFEM. As mentioned in the previous sections, an iterative loop was implemented to allow mesh refinement at each propagation step. After the crack nucleation location and orientation were identified, an initial elliptical crack with semilength $a0 = 0.5\,\text{mm}$ was introduced into the model to start the XFEM-based propagation analysis. This initial crack size was selected as a small numerical defect, sufficiently limited with respect to the gear face width, in order to approximate the early propagation stage without imposing a crack extending through the entire thickness of the gear. The use of an assumed initial crack size represents a modeling approximation, since the exact crack size at the end of the nucleation phase could not be directly determined from the available experimental measurements.

Each step consists of simulating the cyclic loading of the cracked configuration. The stresses evaluated at the crack tip were then used to drive crack propagation according to the Paris law, reported in Equation (6).

$$\frac{da}{dN} = C(\Delta K)^m \tag{2}$$

Once the crack has propagated, the mesh is further refined in the regions of interest to ensure higher computational accuracy in the subsequent stages. After completing this procedure, the updated crack geometry together with the refined mesh is employed to repeat the FEM analysis and propagation cycle, until a critical step corresponding to component failure is reached.

The developed code allows the specification of a maximum crack growth increment per step. As output, the model provides the number of cycles required to reach such propagation. The iterative loop was terminated when the number of cycles required to produce a crack increment of $\Delta da_{\max}$ approached unity (i.e., approximately one cycle), indicating that failure would occur without the need for further cyclic loading. To reduce the computational cost, a mesh de-refinement strategy was also adopted in regions no longer affected by crack propagation, in order to avoid an excessive increase in the computational burden of the simulation. This procedure is described in detail in Appendix. At the end of both stages, the sum of the cycles associated with crack nucleation and propagation provides the final numerical estimation of the fatigue life of the component.

5 | Results

In this section, the results obtained from the adopted numerical approach were combined with thermal dissipations derived from the experimental STBF tests.

14602695, 0, Downloaded from https://onlinelibrary.wiley.com/doi/10.1111/ffe.70431 by Luca Corsaro - Politecnico Di Torino Sist. Bibl Del Polit Di Torino , Wiley Online Library on [08/10/2026]. See the Terms and Conditions (https://onlinelibrary.wiley.com/terms-and-conditions) on Wiley Online Library for rules of use; OA articles are governed by the applicable Creative Commons License

First, the tooth root stresses computed through FEM analysis were compared with the theoretical values calculated according to the relevant standard [39].

Table 3 reports the results for each case study (Gear 1, Gear 2, and Gear 3 in the first column) and for each testing condition (Load 1 and Load 2 in the second column). The reported values are referred to the theoretical tooth root stress calculated according to Standard (ISO 6336 – Part 3 [39], see third column) and those obtained from the FEM simulations (3D XFEM, see fourth column). Then, an error in the computation is reported (error, see fifth column). As can be observed, the differences with respect to the FEM results do not exceed 5%. These relatively small discrepancies may be attributed to surface effects or modeling simplifications that cannot be fully captured within the numerical analysis.

The overall fatigue life of the component was estimated and compared with the experimentally measured fatigue life of the gears.

The main results concerning the crack process are presented in Table 4. The results are reported for each case study (Gear 1, Gear 2, and Gear 3 in the first column) and for each testing condition (Load 1 and Load 2 in the second column). The number of fatigue cycles involved in the nucleation (N°cycles – nucleation [numerical result], see third column) and propagation (N°cycles – propagation [numerical result], see fourth column) phases were evaluated from numerical models (see Section 4). Then, the corresponding number of cycles at which failure occurs (N°cycles – failure [experimental result], see fourth column) was experimentally obtained from STBF tests. The first ratio presented in the Table 4 (ratio nucleation vs. failure, see fifth column) represents the fraction of the nucleation phase with respect to the total fatigue life. On the other hand, the second ratio (ratio total life vs. failure, see sixth column) represents the value between the numerical prediction of failure and the corresponding experimental fatigue life to failure. A value below 100% indicates a conservative prediction, meaning that the component is predicted to fail earlier in the simulation than in the real test; conversely, a value above 100% indicates that failure is predicted later than experimentally observed. From the analysis of Table 4, the following considerations can be drawn. It can be observed that there is a discrepancy in the number of fatigue cycles that led to the failure of Gear 2. The reason was attributed to the slight difference between the two testing conditions, Load 116,500 N and Load 217,000 N, respectively. In all cases except one, crack nucleation accounts for the predominant portion of the overall fatigue life (see ratio failure vs. nucleation), as documented in literature [53]. Furthermore, the numerical model provides conservative predictions with respect to the number of cycles associated with the propagation phase (see fifth column, ratio failure vs. total life). In particular, the component was predicted to fail slightly earlier than observed in the experimental tests. For all cases, except for Gear 2 – Load 2, there was good agreement between the numerical and experimental results. The maximum discrepancy was found in the aforementioned case, where the numerical model predicts only about 20% of the actual fatigue life of the component. For all other cases, a satisfactory correlation was obtained, generally with conservative predictions compared to the experimental tests.

Moreover, the numerical results in terms of the actual crack nucleation location were evaluated. The nucleation points obtained from the proposed numerical approach (3D FEM + SWT, see Section 4.2) was in agreement with that expected along the face width of the geometry (see orange point in Section 2).

The results obtained from thermal dissipations analysis are now presented. The temperature evolution profiles, in term of ΔT, were processed following the procedure outlined in Sections 3.2 and 3.3.

TABLE 3 | Tooth root stress analysis.

Case study	Testing condition	ISO 6336 – part 3 [39] (MPa)	3D XFEM (MPa)	Error (%)
Gear 1	Load 1	1089	1124	3.26
	Load 2	1210	1260	4.17
Gear 2	Load 1	998	1039	4.12
	Load 2	1028	1054	2.52
Gear 3	Load 1	1243	1305	4.96
	Load 2	1315	1384	5.22

TABLE 4 | Crack process: nucleation, propagation and failure.

Case study	Testing condition	N°cycles nucleation (numerical model) (cycle)	N°cycles propagation (numerical model) (cycle)	N°cycles – failure (experimental result) (cycle)	Ratio nucleation vs. failure (%)	Ratio total life vs. failure (%)
Gear 1	Load 1	102,201	5012	125,275	82	86
	Load 2	42,001	3249	46,927	90	96
Gear 2	Load 1	67,801	6906	74,893	91	100
	Load 2	56,301	9119	86,598	65	76
Gear 3	Load 1	152,701	12,197	185,121	82	89
	Load 2	87,001	3497	93,203	93	97

14602695, 0, Downloaded from https://onlinelibrary.wiley.com/doi/10.1111/ffe.70431 by Luca Corsaro - Politecnico Di Torino Sist. Bibl Del Polit Di Torino , Wiley Online Library on [08/10/2026]. See the Terms and Conditions (https://onlinelibrary.wiley.com/terms-and-conditions) on Wiley Online Library for rules of use; OA articles are governed by the applicable Creative Commons License

Figure 7 illustrates the results obtained from Gear 1, presented for each loading condition (see Load 1 and Load 2). As illustrated in Figure 7, the left side of each box (see Temperature evolutions) reports the ΔT extracted from the thermogram of each side (Side 1 and Side 2) of the gear under study. The green colors represent results obtained with the lowest load (Load 1), while the red colors refer to the highest load (Load 2). Furthermore, the darkest colors are associated with Side 1, while the lightest colors correspond to Side 2. The number of cycles representative of the crack nucleation, evaluated from numerical models (see Table 4), is reported for each loading condition (see black lines in Figure 4, crack nucleation [numerical model]). A magnified representation of the final portion of the STBF test is also presented in the upper left region of the temperature evolution. Moreover, thermal maps corresponding to selected number of cycles identified along the temperature evolution (see left side of Figure 4, circles reported over the temperature evolution) are shown on the right side of Figure 7. In particular, a thermal map was extracted near the potential number of cycles corresponding to the crack nucleation identified from the numerical model. After that, thermal maps were extracted when temperature variations were detected along the temperature evolution (in terms of deviation from the stable trend or temperature peaks). The analysis was conducted for each side of the gear under study. The following considerations can be drawn from the results obtained for the Gear 1 case study. For each load, different thermal dissipations were shown by the two gear sides during the STBF test. The temperature evolutions near the expected crack nucleation cycles are often not characterized by temperature variations in terms of ΔT increment from the stable trend. In contrast, this is the classical expected phenomenon observed in specimens, where temperature variations (ΔT increment) occurring prior to failure are always indicative of their crack nucleation phase (see Section 3.3). On the other hand, for gears, this aspect was not always distinguishable, as temperature variations during the nucleation phase may quickly dissipate within the geometry or may not be detected on the side of the gear far from the nucleation zone. In fact, as shown in Figure 7, only one temperature evolution showed a variation in terms of ΔT increment close to the possible number of cycles related to crack nucleation

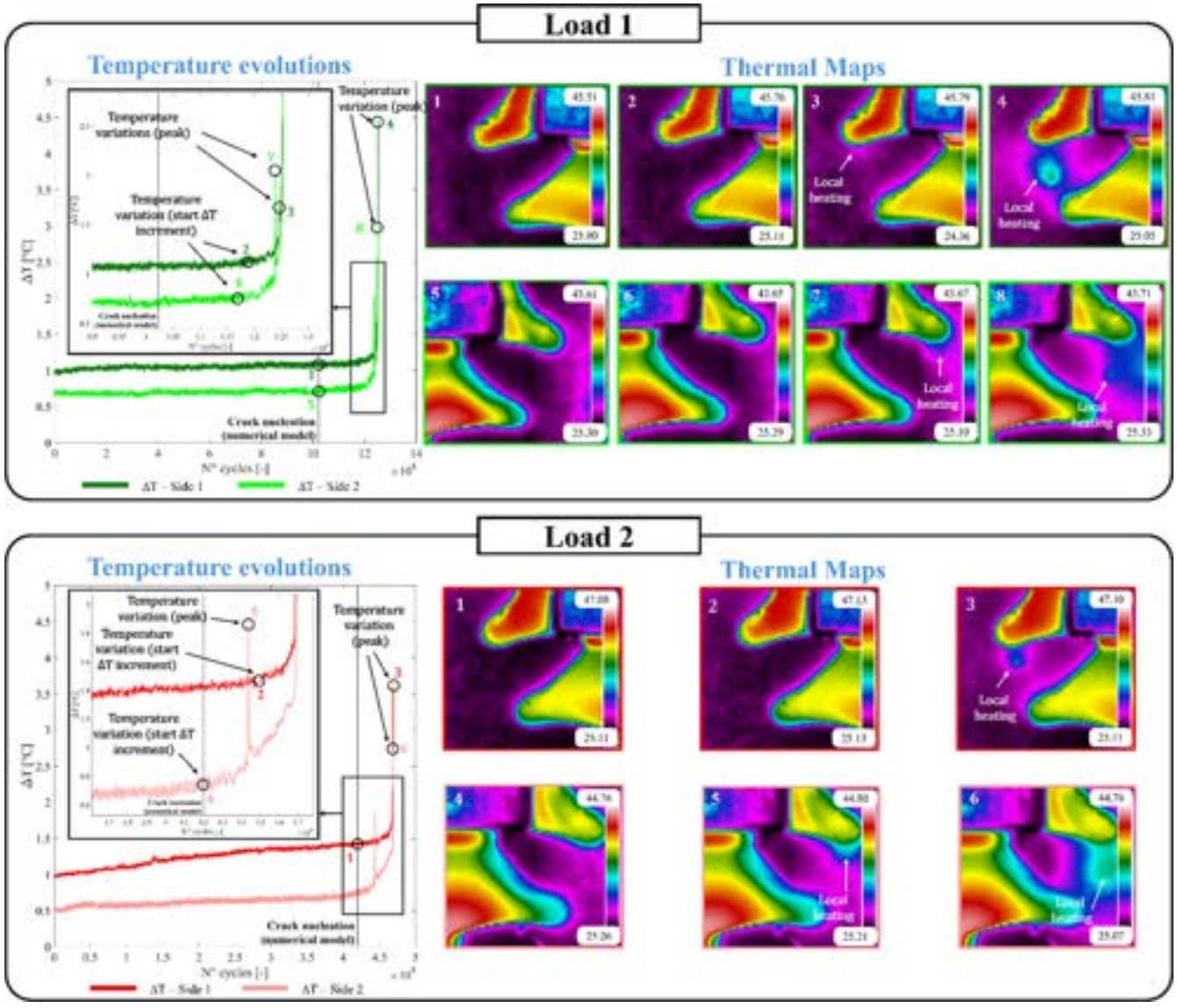

FIGURE 7 | Temperature evolution and thermal maps for Gear 1. [Colour figure can be viewed at wileyonlinelibrary.com]

14602695, 0, Downloaded from https://onlinelibrary.wiley.com/doi/10.1111/ffe.70431 by Luca Corsaro - Politecnico Di Torino Sist. Bibl Del Polit Di Torino , Wiley Online Library on [08/10/2026]. See the Terms and Conditions (https://onlinelibrary.wiley.com/terms-and-conditions) on Wiley Online Library for rules of use; OA articles are governed by the applicable Creative Commons License

(see temperature evolutions on the left side of Figure 7, n°4 in case of Load 2). The other temperature evolutions showed two different behaviors. The first was a relatively stable trend (see temperature evolutions on the left-hand side of Figure 7, n°1 and n°5 in the case of Load 1), suggesting the dissipation of the temperature variation within the geometry. The second consisted of temperature variations occurring immediately after the cycles associated with the nucleation phase and prior to final failure (see temperature evolutions on the left-hand side of Figure 7, n°1 in the case of Load 2), indicating the possible detection from the side opposite to that where the nucleation occurred. Furthermore, no local heating events were detected over the thermal maps corresponding the possible number of cycles representative of the nucleation phase, as a quite uniform temperature field was observed over the tooth (see thermal maps on the right side of Figure 7, n°1 and n°5 in case of Load 1 or n°1 and n°4 in case of Load 2). After the expected nucleation phase, the temperature variations observed in the final part of the test can be divided into two possibilities. The first possibility was the classical deviation from the stable temperature evolution (see left side of Figure 7, temperature variation [start ΔT increment]). In the context of gears, the propagation phase may also contribute for this temperature variation from the stable trend if the ΔT increment occurs after the nucleation phase. This is due to the plastic deformation energy released at the crack tip during its propagation as it approaches the outer sides of the gear, becoming detectable. In this instance, once the temperature variation in terms of ΔT increment was identified (see temperature evolutions on the left side of Figure 7, n°2 and n°6 for Load 1 or n°2 and n°4 for Load 2), the corresponding thermal maps was initially characterized by uniform heating from the tooth under investigation, with no significant local heating (see thermal maps on the right side of Figure 7, n°2 and n°6 for Load 1 or n°2 and n°4 for Load 2). Then, crack propagation was observable from the external lateral sides of the gear only during the final stage of the temperature evolution. Moreover, at this stage, further temperature variations and local heating events became clearly visible. In this case, a second possibility of temperature

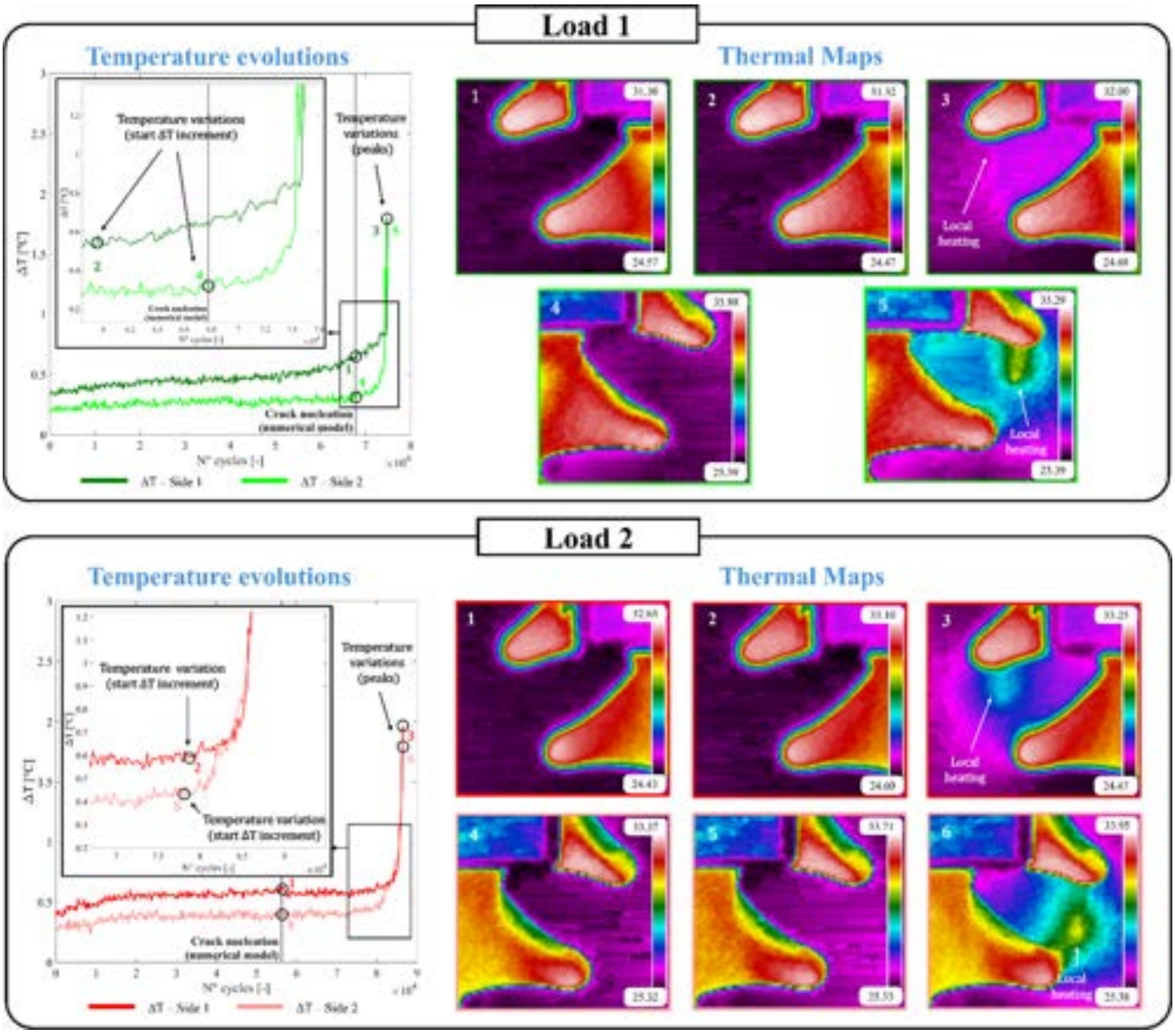

FIGURE 8 | Temperature evolutions and thermal maps for Gear 2. [Colour figure can be viewed at wileyonlinelibrary.com]

14602695, 0, Downloaded from https://onlinelibrary.wiley.com/doi/10.1111/ffe.70431 by Luca Corsaro - Politecnico Di Torino Sist. Bibl Del Polit Di Torino , Wiley Online Library on [08/10/2026]. See the Terms and Conditions (https://onlinelibrary.wiley.com/terms-and-conditions) on Wiley Online Library for rules of use; OA articles are governed by the applicable Creative Commons License

variation was identified along the temperature evolution prior to the occurrence of failure, the presence of peaks, respectively. In particular, this variation may also occur before the final peak associated with failure (see temperature evolutions on the left side of Figure 7, n°3 and n°7 for Load 1 or n°5 for Load 2). In addition, local heating events were identified on thermal maps in proximity to the tooth root zone for this thermal variation (see thermal maps on the right side of Figure 7, n°3 and n°7 for Load 1 or n°5 for Load 2). This phenomenon can be attributed to the nucleation of additional cracks subsequent to the propagation of the initial crack toward the external lateral sides. Subsequent temperature variations corresponding to the peak preceding failure were detected along the temperature evolution, in accordance with the specimens behavior (see temperature evolutions on the left side of Figure 7, n°4 and n°8 for Load 1 or n°3 and n°6 for Load 2). In this case, the local heating reaches its maximum extension just before failure, covering nearly the entire region between the tooth roots of the tooth under test (see thermal maps on the right side of Figure 7, n°4 and n°8 for Load 1 or n°3 and n°6 for Load 2).

Figures 8 and 9 present the results obtained from Gear 2 and Gear 3 case studies, which are illustrated in a manner similar to that of Figure 7 (Gear 1 case study). The following considerations can be pointed out. For the Gear 2 case study, the crack nucleation phase was identified in areas where no temperature variations were observed (Load 2), while ΔT increments were detected prior to the estimated cycles associated with crack nucleation (Side 1 for Load 1). This could be related to the uncertainty in the estimation of the crack process by the numerical model. For Gear 3 (Figure 9), the potential crack nucleation phase was identified close to temperature variations in terms of ΔT increment along the temperature evolution. In particular, these temperature variations occurred at different numbers of cycles on the two sides of the gear. Moreover, the ΔT increment was observed immediately after the crack nucleation phase, which may be directly related to this phase. Consequently, temperature variations observed on the opposite gear side can be attributed to crack propagation toward the external side opposite to the nucleation location. In any case, no local heating events were detected over thermal maps in proximity when the crack nucleation phase was expected for almost

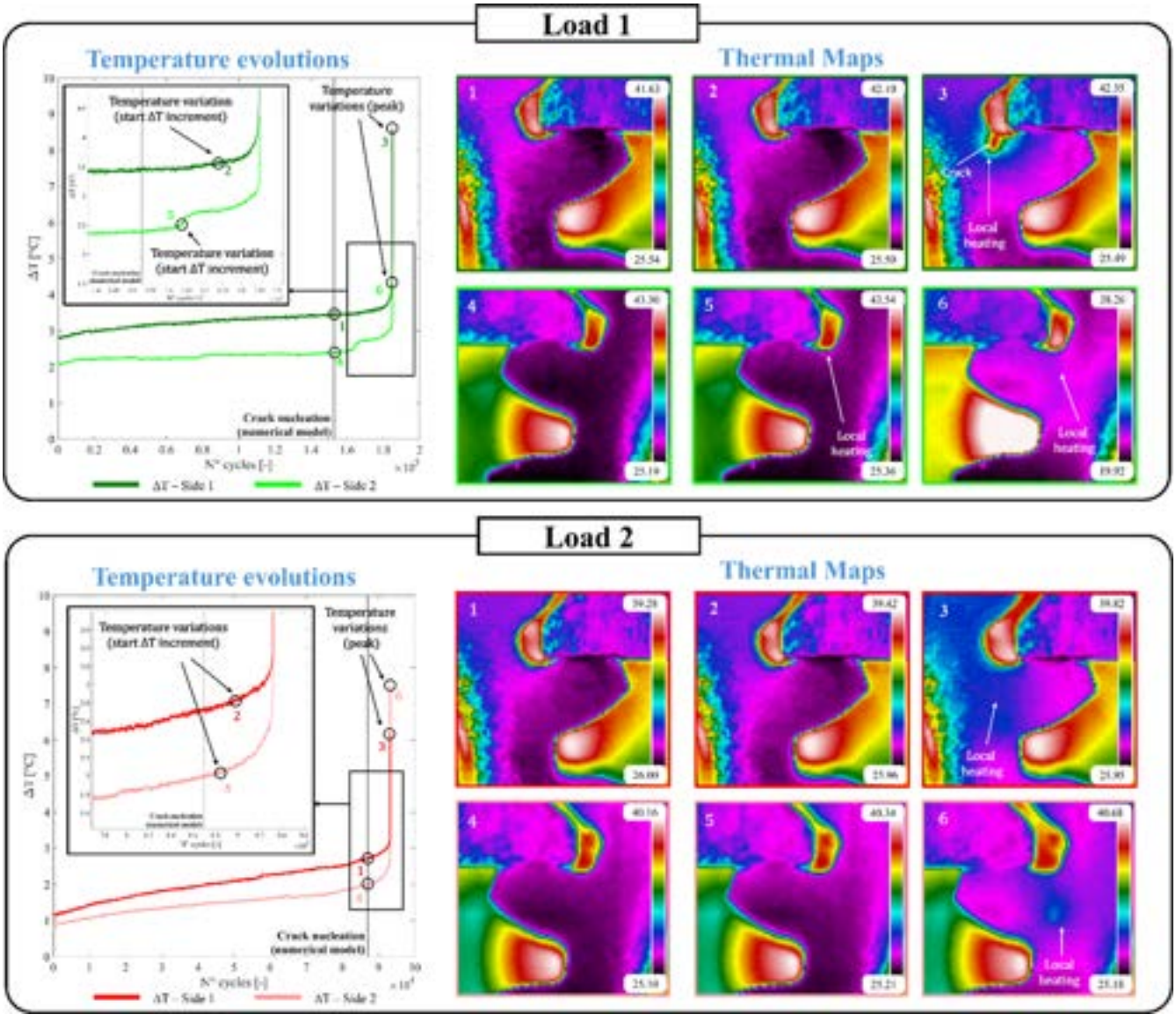

FIGURE 9 | Temperature evolutions and thermal maps for Gear 3. [Colour figure can be viewed at wileyonlinelibrary.com]

14602695, 0, Downloaded from https://onlinelibrary.wiley.com/doi/10.1111/ffe.70431 by Luca Corsaro - Politecnico Di Torino Sist. Bibl Del Polit Di Torino , Wiley Online Library on [08/10/2026]. See the Terms and Conditions (https://onlinelibrary.wiley.com/terms-and-conditions) on Wiley Online Library for rules of use; OA articles are governed by the applicable Creative Commons License

all the investigated case studies. However, for Load 1 of the Gear 3 case study, a significant ΔT increment was observed immediately after the expected nucleation phase (see temperature evolutions on the left-hand side of Figure 9, n°5 for Load 1). This variation also led to local heating at the tooth root (see thermal maps on the right side of Figure 9, n°5 for Load 1). For both Gear 2 and Gear 3, the crack propagation became visible only during the final part of the STBF tests, as also observed for Gear 1 (Figure 7). More in detail, temperature variations in terms of peak preceding failure occurred on the temperature evolution. Furthermore, local heating events appeared near the tooth root immediately after the ΔT increment preceding failure. Their size progressively increased, reaching a maximum just before failure and covering nearly the entire region between the tooth roots of the tested tooth. The only observed difference was the presence of a single peak along the temperature evolution, instead of multiple temperature variations in terms of peaks, prior to those related to failure. It is important to note that the Gear 2 case study exhibited an anomalous number of fatigue cycles to failure in the experimental tests, as it was lower for the lowest load. In any case, the behavior of thermal dissipations during crack evolution was analyzed to investigate how temperature variations and local heating events can be used to describe the phenomena under study.

The previous considerations obtained from the case studied (Gear 1, Gear 2, and Gear 3) showed that the investigation of crack process may be conducted independently of the magnitude reached during the STBF test, by focusing exclusively on the profile of the temperature evolution itself. This was supported by the clear similarities observed in the thermal dissipation behavior compared with specimens (see Section 3.3). Consequently, the crack process was investigated along the temperature evolution by considering ΔT increments from the stable trend or peaks phenomena. Based on the observed results for all the investigated

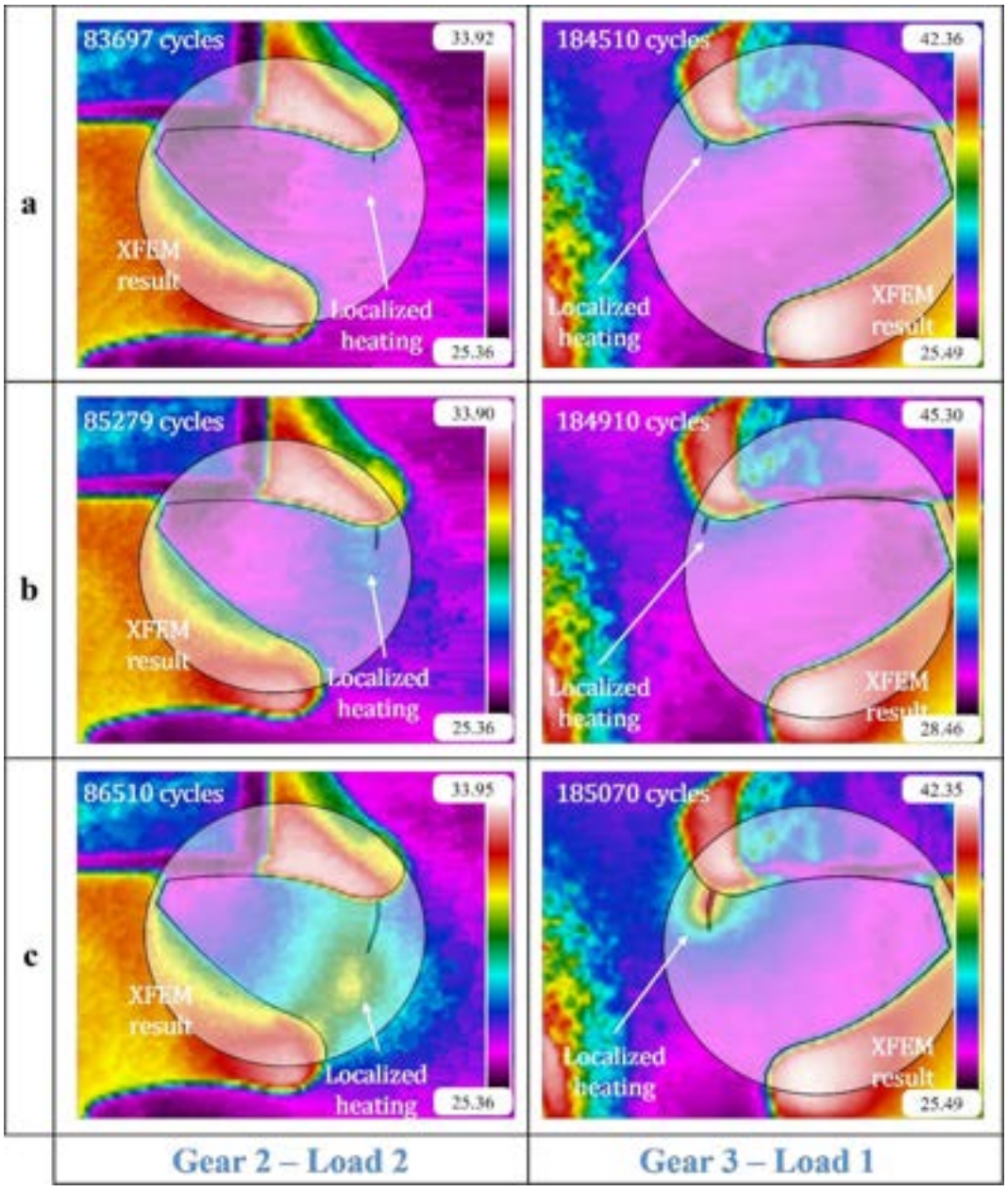

FIGURE 10 | Crack path comparison before failure. [Colour figure can be viewed at wileyonlinelibrary.com]

14602695, 0, Downloaded from https://onlinelibrary.wiley.com/doi/10.1111/ffe.70431 by Luca Corsaro - Politecnico Di Torino Sist. Bibl Del Polit Di Torino , Wiley Online Library on [08/10/2026]. See the Terms and Conditions (https://onlinelibrary.wiley.com/terms-and-conditions) on Wiley Online Library for rules of use; OA articles are governed by the applicable Creative Commons License

case studies, the detection of crack tip propagation can be described through the combined analysis of temperature evolutions and thermal maps. In particular, deviations from the quite stable thermal trend are associated with the progressive approach of the crack tip toward the external sides of the gear, as a consequence of increasing energy dissipation at the crack tip, which produces a nearly uniform heating at the tooth root zone. At the same time, thermal maps provide spatial information: Localized heating events become clearly detectable only when the crack tip is sufficiently close to the external surfaces, progressively outlining the

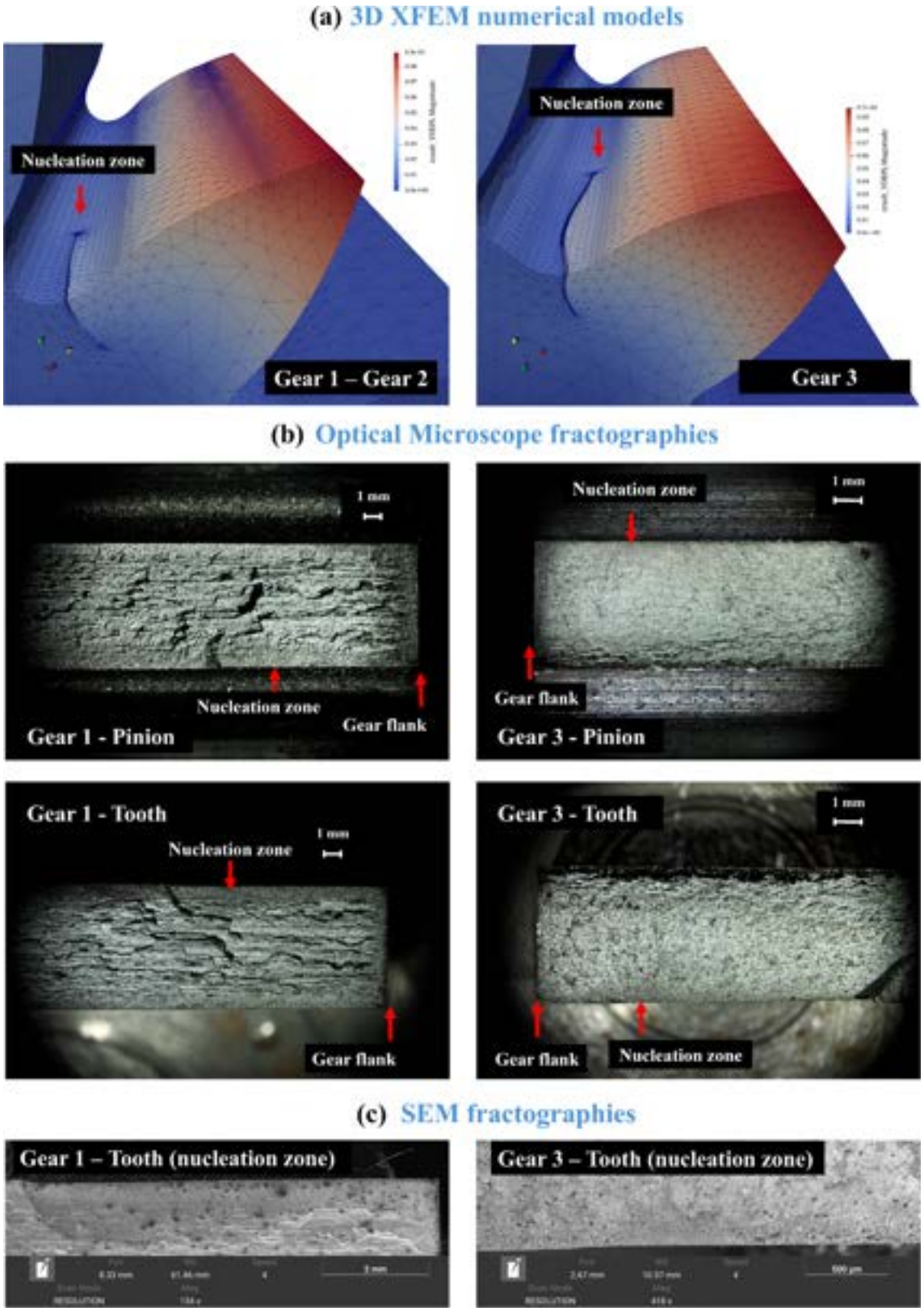

FIGURE 11 | Crack process comparison: numerical results and fractographic analysis. [Colour figure can be viewed at wileyonlinelibrary.com]

14602695, 0, Downloaded from https://onlinelibrary.wiley.com/doi/10.1111/ffe.70431 by Luca Corsano - Politecnico Di Torino Sist. Bibl Del Polit Di Torino , Wiley Online Library on [08/10/2026]. See the Terms and Conditions (https://onlinelibrary.wiley.com/terms-and-conditions) on Wiley Online Library for rules of use; OA articles are governed by the applicable Creative Commons License

crack path up to final failure. This combined approach allows for the identification of crack propagation even when the crack is not yet directly visible on the external surface.

A further analysis related to the crack path evolution was also carried out. More in detail, a comparative analysis was conducted between thermal maps and numerical results, considering three distinct number of cycles. The analysis was performed on the later face of the gear where the crack was well visible through thermal phenomena. Figure 10 shows the results for two case studies with different gear geometries, Gear 2 and Gear 3, respectively. The analysis is reported for two representative load conditions. The initial investigation focused on a number of cycles at which the crack became visible on the thermogram at the external lateral face of the gear (see Figure 10, letter a). The second thermal map under consideration was a number of cycles between the previous one and that related to the gear failure (see Figure 10, letter b). Finally, the last available thermal map prior to the failure was analyzed (see Figure 10, letter c). The numerical results, in the form of circular shaded images representing the crack path evolution, were extracted from the final stage of the crack propagation simulation and then positioned on the corresponding thermal map. From the analysis of Figure 10, the evolution of the crack process was evident through distinguishable thermal dissipations within the gear. This was characterized by localized heating in proximity to the crack location, particularly at the tooth root zone. This phenomenon became more pronounced as the crack evolved toward the lateral face of the gear, in agreement with the XFEM results. Furthermore, the maximum crack path evolution well matched with the numerical model, as the thermal dissipations clearly highlighted the crack location at the tooth root. Moreover, the last thermal map detected for the Gear 3 case study (see Figure 10, letter c for Gear 3 – Load 1) corresponded to the number of cycles at which the crack extends along the entire face width of the gear, immediately prior to failure.

As an example, Figure 11 compares the crack process predicted by 3D XFEM numerical models (see Figure 11a) with the corresponding fractographic observations (see Figure 11b,c). Figure 11b,c shows the fractographies of Gear 1 and Gear 3, highlighting the fracture surfaces of both teeth and pinions. The fracture surfaces mainly reveal two classical distinct regions: a fatigue crack propagation zone and the area associated to the final fracture. No clear beach marks were observed, probably due to the high load levels applied during the STBF tests. On contrary, ratchet marks were visible, confirming the presence of high tensile stresses [40, 57]. The observed fracture patterns indicate an asymmetric crack nucleation along the face width, leading to a nonuniform crack propagation across the tooth section. These results also consistent with the asymmetric thermal dissipations observed from the two lateral sides of the gear and in agreement with the results of the numerical model.

6 | Conclusions

In this study, the combination of IR Thermography and 3D XFEM numerical models was adopted for the investigation of crack mechanisms in gears. The investigation was conducted for three different case studies, incorporating both experimental activities and numerical models.

The experimental results showed that the crack process in gears can be effectively investigated through thermal dissipations, analyzed in terms of temperature evolutions and local heating events. In particular, the study highlighted that crack nucleation is not always directly detectable from temperature variations, due to the three-dimensional geometry of the component and the position of the nucleation zone within the face width. On the other hand, crack propagation becomes progressively more evident through deviations from both quite stable thermal trend and appearance of localized heating, especially when the crack tip approaches the external surfaces.

The numerical analysis, based on a 3D XFEM framework combined with a critical plane fatigue criterion and the crack propagation governed by the Paris law, provided useful support for the interpretation of experimental observations. In particular, the model enabled the estimation of crack nucleation location and propagation path.

The comparison between numerical predictions and experimental evidence confirmed the asymmetric crack propagation along the face width and the capability of the proposed approach to describe the crack process even when the crack is still internal and not directly noticeable. Fractographic analysis further supported these findings by revealing fracture patterns consistent with thermal dissipations and numerical predictions, particularly in terms of asymmetric crack nucleation and nonuniform propagation along the tooth section. It is important to note that the aim of the present work was to investigate the evolution of the crack process through the thermal dissipations and to assess the capability of the proposed combined experimental–numerical approach for crack process analysis in gears under STBF conditions. In this context, the experimental investigation was conducted on a limited number of case studies and tests, as it was intended to support the methodological development rather than a statistical fatigue characterization. In addition, the numerical model was based on a simplified material representation. In particular, the residual stress fields induced by the carburizing process were not included, and the gradient of mechanical properties due to the case-hardened layer was not explicitly modeled. These aspects may influence both crack initiation and propagation behavior and should be considered in future developments.

Overall, the proposed methodology demonstrates the potential of combining IR Thermography with numerical modeling for the investigation of fatigue crack processes in real mechanical components. The approach can support the identification and interpretation of crack evolution, providing a useful tool for further studies aimed at improving the understanding of fatigue behavior in gears.

Nomenclature

a	semilength of the initial crack (mm)
b	fatigue strength exponent (–)
c	fatigue ductility exponent (–)

14602695, 0, Downloaded from https://onlinelibrary.wiley.com/doi/10.1111/ffe.70431 by Luca Corsaro - Politecnico Di Torino Sist. Bibl Del Polit Di Torino , Wiley Online Library on [08/10/2026]. See the Terms and Conditions (https://onlinelibrary.wiley.com/terms-and-conditions) on Wiley Online Library for rules of use; OA articles are governed by the applicable Creative Commons License

C	Paris law coefficient (MPa$\sqrt{\text{m}}$)
$da_{\max}$	maximum advancement per cycle (mm)
E	Young's modulus (MPa)
H	surface tooth root hardness (HV)
$h_{\max}$	maximum element size in refined mesh (mm)
m	Paris law exponent (–)
m_{n}	normal modulus
n	number of iterations (–)
N	number of cycles (–)
R	load ratio ($F_{\min}/F_{\max}$) (_)
Rz	tooth root roughness (Rz)
w	face width (mm)
x	shift profile, x (–)
Y_{F}	tooth form factor (–)
Y_{S}	stress correction factor (–)
z	number of teeth (–)
α	pressure angle (°)
σ'_f	fatigue strength coefficient (MPa)
$\sigma_{n,max}$	maximum normal stress on the critical plane (MPa)
ΔK	Stress intensity factor range (MPa$\sqrt{\text{m}}$)
$\Delta\epsilon_{n,max}$	Maximum normal strain range on the critical plane (–)
ϵ'_f	Fatigue ductility coefficient (–)
$\frac{da}{dN}$	crack growth rate (mm/cycle)

Data Availability Statement

Data are available on request from the authors.

References

1. N. Levy and J. R. Rice, "Local Heating by Plastic Deformation at a Crack Tip," in *Physics Strength and Plasticity*, ed. A. S. Argon (MIT Press, 1969), 277–293.

2. R. Attermo and G. Östberg, "Measurements of the Temperature Rise Ahead of a Fatigue Crack," *International Journal of Fracture Mechanics* 7 (1971): 122–124.

3. P. J. Loos and F. R. Brotzen, "Localized Heat Generation During Fracture Cyclically Loaded Steel," *Metallurgical Transactions A* 14, no. 7 (1983): 1409–1419.

4. O. Plekhow, T. Palin-Luc, N. Saintier, S. Uvarow, and O. Naimark, "Fatigue Crack Initiation and Growth in a 35CrMo4 Steel Investigated by Infrared Thermography," *Fatigue & Fracture of Engineering Materials & Structures* 28, no. 1–2 (2005): 169–178.

5. D. Wagner, N. Ranc, C. Bathias, and P. C. Paris, "Fatigue Crack Initiation Detection by an Infrared Thermography Method," *Fatigue and Fracture of Engineering Materials and Structures* 33, no. 1 (2010): 12–21.

6. H. X. Zhang, C. Y. Wei, Z. F. Yan, W. X. Wang, S. F. Guo, and Y. G. Zhou, "Research on Fatigue Crack Propagation Behaviour of 4003 Ferritic Stainless Steel Based on Infrared Thermography," *Fatigue and Fracture of Engineering Materials and Structures* 39, no. 2 (2016): 206–216.

7. V. Crupi, G. Epasto, E. Guglielmino, and G. Risitano, "Analysis of Temperature and Fracture Surface of AISI4140 Steel in Very High Cycle Fatigue Regime," *Theoretical and Applied Fracture Mechanics* 80 (2015): 22–30.

8. D. Kujawski and A. Ellyin F, "A Fatigue Crack Propagation Model," *Engineering Fracture Mechanics* 20, no. 5 (1984): 695–704.

9. N. Ranganathan, K. Jendoubi, M. Benguediab, and J. Petit, "Effect of R Ratio and ΔK Level on the Hysteretic Energy Dissipated During Fatigue Crack Propagation," *Scripta Metallurgica* 21, no. 8 (1987): 1045–1049.

10. C. E. Turner and O. Kolednik, "Application of Energy Dissipation Rate Arguments to Stable Crack Growth," *Fatigue and Fracture of Engineering Materials and Structures* 17, no. 10 (1994): 1109–1127.

11. C. E. Turner and O. Kolednie, "A Micro and Macro Approach to the Energy Dissipation Rate Model of Stable Ductile Crack Growth," *Fatigue and Fracture of Engineering Materials and Structures* 17, no. 9 (1994): 1089–1107.

12. R. P. Skelton, T. Vilhelmsen, and G. A. Webster, "Energy Criteria and Cumulative Damage During Fatigue Crack Growth," *International Journal of Fatigue* 20, no. 9 (1998): 641–649.

13. K. N. Pandey and S. Chand, "Analysis of Temperature Distribution Near the Crack Tip Under Constant Amplitude Loading," *Fatigue and Fracture of Engineering Materials and Structures* 31, no. 5 (2008): 316–326.

14. D. Cojocaru and A. M. Karlsson, "Assessing Plastically Dissipated Energy as a Condition for Fatigue Crack Growth," *International Journal of Fatigue* 31, no. 7 (2009): 1154–1162.

15. A. Y. Fedorova, M. V. Bannikov, O. A. Plekhov, and E. V. Plekhov, "Infrared Thermography Study of the Fatigue Crack Propagation," *Frattura ed Integrità Strutturale* 6, no. 21 (2012): 46–53.

16. H. Q. Nguyen, L. Gallimard, and C. Bathias, "Numerical Simulation of the Coupling Between Thermal Dissipation and Fish-Eye Crack Growth in Very High Cycle Fatigue Regime," *Fatigue and Fracture of Engineering Materials and Structures* 36, no. 5 (2013): 450–461.

17. N. Ranc, T. Palin-Luc, P. C. Paris, and N. Saintier, "About the Effect of Plastic Dissipation in Heat at the Crack Tip on the Stress Intensity Factor Under Cyclic Loading," *International Journal of Fatigue* 58, no. 58 (2014): 56–65.

18. G. Meneghetti and M. Ricotta, "Evaluating the Heat Energy Dissipated in a Small Volume Surrounding the Tip of a Fatigue Crack," *International Journal of Fatigue* 92 (2016): 605–615.

19. E. Feng, X. Wang, and C. Jiang, "Multiaxial Fatigue Evaluation of Type 316L Stainless Steel Based on Critical Plane and Energy Dissipation," *Fatigue and Fracture of Engineering Materials and Structures* 45, no. 12 (2022): 3486–3499.

20. R. Jones, M. Krishnapillai, K. Cairns, and N. Matthews, "Application of Infrared Thermography to Study Crack Growth and Fatigue Life Extension Procedures," *Fatigue and Fracture of Engineering Materials and Structures* 33, no. 12 (2010): 871–884.

21. S. Hwang, Y. K. An, J. M. Kim, and H. Sohn, "Monitoring and Instantaneous Evaluation of Fatigue Crack Using Integrated Passive and Active Laser Thermography," *Optics and Lasers in Engineering* 119 (2019): 9–17.

22. F. Curà, A. Mura, and L. Corsaro, "Experimental Investigation on Crack Propagation Paths in Spur Gears," *IOP Conference Series: Materials Science and Engineering* 1214, no. 1 (2022): 12029.

23. F. Curà, A. Mura, and C. Rosso, "Effect of Rim and Web Interaction on Crack Propagation Paths in Gears by Means of XFEM Technique," *Fatigue and Fracture of Engineering Materials and Structures* 38, no. 10 (2015): 1237–1245.

24. Y. Wei and Y. Jiang, "Fatigue Fracture Analysis of Gear Teeth Using XFEM," *Transactions of Nonferrous Metals Society of China* 29, no. 10 (2019): 2099–2108.

14602695, 0, Downloaded from https://onlinelibrary.wiley.com/doi/10.1111/ffe.70431 by Luca Corsaro - Politecnico Di Torino Sist. Bibl Del Polit Di Torino , Wiley Online Library on [08/10/2026]. See the Terms and Conditions (https://onlinelibrary.wiley.com/terms-and-conditions) on Wiley Online Library for rules of use; OA articles are governed by the applicable Creative Commons License

25. M. S. Raghav, A. Singh, and S. Patel, "Fault Analysis of Spur Gear Using XFEM," *Engineering Failure Analysis* 134, no. 106060 (2022): 106060.

26. D. G. Lewicki and R. Ballarini, "Effect of Rim Thickness on Gear Crack Propagation Path," *Journal of Mechanical Design* 119 (1997): 88–95.

27. A. M. Alshoaibi, "Fatigue Crack Growth Analysis Under Constant Amplitude Loading Using Finite Element Method," *Materials* 15, no. 8 (2022): 2937.

28. R. Thirumurugan and N. Gnanasekar, "Influence of Finite Element Model, Load-Sharing and Load Distribution on Crack Propagation Path in Spur Gear Drive," *Engineering Failure Analysis* 110, no. 104383 (2020): 104383.

29. T. Belytschko and T. Black, "Elastic Crack Growth in Finite Elements With Minimal Remeshing," *International Journal for Numerical Methods in Engineering* 45, no. 5 (1999): 601–620.

30. M. R. Nikfam, M. Zeinoddini, F. Aghebati, and A. A. Arghaei, "Experimental and XFEM Modelling of High Cycle Fatigue Crack Growth in Steel Welded T-Joints," *International Journal of Mechanical Sciences* 153 (2019): 178–193.

31. M. Kiani and G. T. Fry, "Fatigue Analysis of Railway Wheel Using a Multiaxial Strain-Based Critical-Plane Index," *Fatigue and Fracture of Engineering Materials and Structures* 41, no. 2 (2018): 412–424.

32. S. L. Sunde, F. Berto, and B. Haugen, "Efficient Implementation of Critical Plane for 3D Stress Histories Using Triangular Elements," *International Journal of Fatigue* 134 (2020): 105448.

33. A. Laamouri, H. Sidhom, and C. Braham, "A Predictive Methodology for High-Cycle Fatigue Behavior of Machined Metallic Parts," *Journal of Materials Engineering and Performance* 31, no. 6 (2022): 4776–4794.

34. W. N. Findley, "A Theory for the Effect of Mean Stress on Fatigue of Metals Under Combined Torsion and Axial Load or Bending Brown University: Engineering Materials Research Laboratory, Division of Engineering," (1958).

35. B. Crossland, "Effect of Large Hydrostatic Pressures on the Torsional Fatigue Strength of an Alloy Steel," The Third International Conference on Fatigue of Metals (1956): 138 12.

36. A. Fatemi and D. F. Socie, "A Critical Plane Approach to Multiaxial Fatigue Damage Including Out-Of-Phase Loading," *Fatigue and Fracture of Engineering Materials and Structures* 11, no. 3 (1988): 149–165.

37. D. F. Socie, "Multiaxial Fatigue Damage Models," *Journal of Engineering Materials and Technology* 109, no. 4 (1987): 293–298.

38. K. Smith, "A Stress-Strain Function for the Fatigue of Metals," *Journal of Materials* 5 (1970): 767–778.

39. International Organization for Standardization, "ISO 6336-3:2019. Calculation of Load Capacity of Spur and Helical Gears — Part 3: Calculation of Tooth Bending Strength Geneva ISO," (2019).

40. American National Standards Institute/American Gear Manufacturers Association, "ANSI/AGMA 1010-F14. Appearance of Gear Teeth — Terminology of Wear and Failure Alexandria, VA AGMA," (2020).

41. L. Bonaiti and C. Gorla, "Gear Tooth Root Bending Strength Estimation Under the Assumption of Fatigue Limit Existence," *Material Design & Processing Communications* 2022 (2022): 1–13.

42. L. Bonaiti, A. B. M. Bayoumi, F. Concli, F. Rosa, and C. Gorla, "Gear Root Bending Strength: A Comparison Between Single Tooth Bending Fatigue Tests and Meshing Gears," *Journal of Mechanical Design* 143, no. 10 (2021): 103402.

43. S. Li, "Finite Element Analyses for Contact Strength and Bending Strength of a Pair of Spur Gears With Machining Errors, Assembly Errors and Tooth Modifications," *Mechanism and Machine Theory* 42, no. 1 (2007): 88–114.

44. M. L. Roessle and A. Fatemi, "Strain-Controlled Fatigue Properties of Steels and Some Simple Approximations," *International Journal of Fatigue* 22, no. 6 (2000): 495–511.

45. N. Shamsaei and A. Fatemi, "Effect of Hardness on Multiaxial Fatigue Behaviour and Some Simple Approximations for Steels," *Fatigue and Fracture of Engineering Materials and Structures* 32, no. 8 (2009): 631–646.

46. X. Sun, J. Zhao, S. Song, Y. Lu, and H. Sun, "A Numerical Model for Total Bending Fatigue Life Estimation of Carburized Spur Gears Considering the Hardness Gradient and Residual Stress," *Meccanica* 59 (2024): 1037–1060.

47. S. Xianshun, Z. Jun, H. Youbin, et al., "The Prediction and Experimental Study of Bending Fatigue Life of Carburized Gears," *Journal of Materials Engineering and Performance* 33 (2024): 1051–1059.

48. I. Čular, K. Vučković, D. Žeželj, and S. Glodež, "Analytical Approach for Low and High Cycle Bending Fatigue Life Prediction of Carburized Gear Steel Specimens," *Engineering Failure Analysis* 108 (2020): 104328.

49. I. Čular, I. Galić, R. Mašović, and K. Vučković, "The Effect of Gear Module on Bending Fatigue Failure Location in Carburized and Shot-Peened Spur Gears," *International Journal of Fatigue* 196 (2025): 108901.

50. FLIR Thermal Camera User's Manual, A6700sc/A6750sc.

51. G. Gasparini, U. Mariani, C. Gorla, M. Filippini, and F. Rosa, "Bending Fatigue Tests of Helicopter Case Carburized Gears: Influence of Material, Design and Manufacturing Parameters," Fall Technical Meeting American Gear Manufacturers Association (AGMA). (2008): 131 142.

52. C. Gorla, F. Rosa, F. Concli, and H. Albertini, "Bending Fatigue Strength of Innovative Gear Materials for Wind Turbines Gearboxes: Effect of Surface Coatings American Society of Mechanical Engineers (ASME) International Mechanical Engineering Congress and Exposition," (2012): 45233 3141 3147.

53. S. S. Samant, V. B. Pandey, I. V. Singh, and R. N. Singh, "Effect of Double Austenitization Treatment on Fatigue Crack Growth and High Cycle Fatigue Behavior of Modified 9Cr–1Mo Steel," *Materials Science and Engineering A-Structural Materials Properties Microstructure and Processing* 788 (2020): 139495.

54. S. Mobasher Moghaddam, J. A. R. Bomidi, F. Sadeghi, N. Weinzapfel, and A. Liebel, "Effects of Compressive Stresses on Torsional Fatigue," *Tribology International* 77 (2014): 196–210.

55. X. M. Chen, Q. Sun, D. Guan, and F. P. A. Yang, "A Continuum Damage Mechanics Approach for Fatigue Life Prediction of Open-Hole Metallic Plate," *Applied Mechanics and Materials* 1060 (2014): 670–671.

56. M. Sistaninia and M. Niffenegger, "Prediction of Damage-Growth Based Fatigue Life of Polycrystalline Materials Using a Microstructural Modeling Approach," *International Journal of Fatigue* 66 (2014): 118–126.

57. ISO 10825, "Gears - Wear and Damage to Gear Teeth. Part 1: Nomenclature and Characteristics," (2022).

14602695, 0, Downloaded from https://onlinelibrary.wiley.com/doi/10.1111/ffe.70431 by Luca Corsaro - Politecnico Di Torino Sist. Bibl Del Polit Di Torino , Wiley Online Library on [08/10/2026]. See the Terms and Conditions (https://onlinelibrary.wiley.com/terms-and-conditions) on Wiley Online Library for rules of use; OA articles are governed by the applicable Creative Commons License

Appendix A

ALGORITHM 1 | Fatigue Crack Growth Analysis.

```
Input: Cyclic load parameters (R=0.1), material properties, Paris law constants
Run initial FEM simulation under cyclic load
Extract time-dependent stress and strain tensors
Apply SWT criterion using Python script
Determine crack initiation point and orientation
De ne number of iterations=n
for i=1,. .., n do
  Insert initial crack (elliptical surface, a=0.05mm)
  Refine mesh locally:
     Max element size: h_max=a/10
     Refinement area radius: 2 · da_max
  while local mesh density not sufficient do
    Further local refinement
  end while
  Propagate crack by da_max using FEM simulation
  Compute number of cycles for increment via Paris law
  Update crack orientation and geometry
  while propagation not complete do
     Compute error field near current crack front
     Refine mesh in high-error zones
     Derefine mesh in low-interest regions
     Propagate crack by da_max
     Update cycle count and geometry
  end while
end for
Compute total nucleation cycles (from SWT)
Sum propagation cycles
Output: Total cycles to failure=nucleation + propagation
```

The fatigue crack growth analysis is carried out following the workflow reported in Algorithm 1. The procedure starts with an initial FEM analysis performed under cyclic loading conditions, which is required for the application of the SWT criterion. This preliminary analysis is aimed at identifying both the crack nucleation location and the corresponding critical plane orientation. A cyclic load with a load ratio of $R = 0.1$ is applied, and the time-dependent stress and strain tensors are extracted from the simulation. The load levels adopted in the analysis are derived from a previous experimental campaign conducted to estimate the fatigue limits of the two investigated materials. A dedicated Python script is then employed to apply the SWT criterion and determine the crack nucleation point together with the associated critical plane orientation. Based on this information, an initial crack is automatically inserted into the model at the identified location. The initial defect is defined as an elliptical surface crack with a length of $a = 0.05$ mm. Before performing the first crack propagation step, a local mesh refinement is carried out in the vicinity of the crack. The refinement strategy is defined by imposing a maximum element size equal to $h_{\max} = a/10$ within a surrounding region having a radius equal to $2 \cdot da_{\max}$. The mesh refinement procedure is automatically repeated until the required local mesh density is achieved.

Once the required local mesh density is reached, the first crack propagation step is performed. The crack advance is governed by the predefined maximum increment $da_{\max}$, and the number of cycles required to achieve this increment is computed using the Paris law. In addition to the cycle count, the analysis provides the updated crack geometry and propagation orientation. Following this initial propagation step, the code enters an inner iterative loop in which an error field is evaluated in the vicinity of the current crack front. Based on this error field, the mesh is locally refined in regions characterized by high numerical error, while a de-refinement strategy is simultaneously applied in areas no longer relevant to the crack propagation. This adaptive meshing procedure is adopted to control the computational cost and is repeated until the desired numerical accuracy is achieved. The crack is then propagated again by an increment equal to $da_{\max}$, and both the crack geometry and the corresponding cycle count are updated. This sequence of crack propagation, error field evaluation, mesh refinement and derefinement is repeated until the propagation process is completed, as controlled by the outer loop of the algorithm. At the end of the simulation, the total number of cycles associated with crack nucleation is obtained from the SWT criterion, while the total number of cycles required for crack propagation is computed by summing the cycles corresponding to each propagation step. The sum of these two contributions represents the predicted fatigue life of the component and is finally compared with the experimentally measured number of cycles to failure.

14602695, 0, Downloaded from https://onlinelibrary.wiley.com/doi/10.1111/ffe.70431 by Luca Corsano - Politecnico Di Torino Sist. Bibl Del Polit Di Torino , Wiley Online Library on [08/10/2026]. See the Terms and Conditions (https://onlinelibrary.wiley.com/terms-and-conditions) on Wiley Online Library for rules of use; OA articles are governed by the applicable Creative Commons License